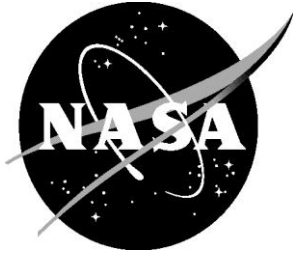# Thermal Modeling and Testing of High-Temperature Refractory Ceramic Insulation Felts

Kamran Daryabeigi,
Langley Research Center, Hampton, Virginia

April 2024

NASA STI Program Report Series

Since its founding, NASA has been dedicated to the advancement of aeronautics and space science. The NASA scientific and technical information (STI) program plays a key part in helping NASA maintain this important role.

The NASA STI program operates under the auspices of the Agency Chief Information Officer. It collects, organizes, provides for archiving, and disseminates NASA's STI. The NASA STI program provides access to the NTRS Registered and its public interface, the NASA Technical Reports Server, thus providing one of the largest collections of aeronautical and space science STI in the world. Results are published in both non-NASA channels and by NASA in the NASA STI Report Series, which includes the following report types:

- TECHNICAL PUBLICATION. Reports of completed research or a major significant phase of research that present the results of NASA Programs and include extensive data or theoretical analysis. Includes compilations of significant scientific and technical data and information deemed to be of continuing reference value. NASA counterpart of peer-reviewed formal professional papers but has less stringent limitations on manuscript length and extent of graphic presentations.

- TECHNICAL MEMORANDUM. Scientific and technical findings that are preliminary or of specialized interest, e.g., quick release reports, working papers, and bibliographies that contain minimal annotation. Does not contain extensive analysis.

- CONTRACTOR REPORT. Scientific and technical findings by NASA-sponsored contractors and grantees.

- CONFERENCE PUBLICATION. Collected papers from scientific and technical conferences, symposia, seminars, or other meetings sponsored or co-sponsored by NASA.

- SPECIAL PUBLICATION. Scientific, technical, or historical information from NASA programs, projects, and missions, often concerned with subjects having substantial public interest.

- TECHNICAL TRANSLATION. English-language translations of foreign scientific and technical material pertinent to NASA's mission.

Specialized services also include organizing and publishing research results, distributing specialized research announcements and feeds, providing information desk and personal search support, and enabling data exchange services.

For more information about the NASA STI program, see the following:

- Access the NASA STI program home page at http://www.sti.nasa.gov

- Help desk contact information:

https://www.sti.nasa.gov/sti-contact-form/
and select the "General" help request type.

NASA/TM–20240003609

Thermal Modeling and Testing of High-Temperature Refractory Ceramic Insulation Felts

Kamran Daryabeigi,
Langley Research Center, Hampton, Virginia

April 2024

Acknowledgements

Available from:

NASA STI Program / Mail Stop 050
NASA Langley Research Center
Hampton, VA 23681-2199

Thermal Modeling and Testing of High-Temperature Refractory Ceramic Fibrous Insulation Felts

Abstract

Heat transfer in high-temperature, high-porosity, flexible refractory ceramic fibrous insulation felts is investigated. Heat transfer in these insulation materials consists of combined gas conduction, solid conduction, and radiation modes, with the precise theoretical modeling of the latter two modes being formidable. A semi-empirical model that requires inverse methods and steady-state thermal test data to infer some of the required model parameters is further developed in this study, and applied to five insulation materials for temperatures between 300 K and 1900 K. The steady-state thermal test setup at NASA Langley Research Center with recent modifications to increase its testing capability to 1900 K is discussed. Design considerations to ensure one-dimensional heat transfer in the test setup are described. Test data and corresponding thermal models for alumina and zirconia-based fibrous insulation felts are presented. Furthermore, test data and thermal models on two fibrous insulation samples containing additives to further suppress either radiation or gas conduction modes of heat transfer are presented. Previously published alumina-based insulation data are also re-processed using the updated modeling methodology. The significance of various heat transfer modes in typical insulation samples is discussed and used to provide general guidance on optimum insulation layups.

Nomenclature

A	cross sectional area, m^2
a_i	coefficients for low-pressure thermal conductivity expression, Eq. (20)
c_i	coefficients for e/n^{*2} expression, Eq. (27)
c_P	specific heat, J.kg^{-1}.K^{-1}
D	average fiber diameter, m
d	gas collision diameter, m
e	specific extinction coefficient, m^2.kg^{-1}
f	fiber volume fraction
F	scaling factor for solid conduction model
Kn	Knudsen number
K_B	Boltzmann constant, 1.3806×10^{-23} J.K^{-1}
k	thermal conductivity, W.m^{-1}.K^{-1}
L	thickness, m
L_i	distance between sample internal thermocouples and water-cooled plate, m
n^*	effective index of refraction
P	pressure, torr
P_r	Prandtl number
q''	heat flux, W.m^{-2}
R	thermal resistance, K.W^{-1}
T	temperature, K

y	spatial coordinate, m
α	thermal accommodation coefficient
β	parameter for gas conduction model
Δ	uncertainty
κ	gas conduction characteristic length (pore size), m
γ	specific heat ratio
λ	molecular mean free path, m
μ	dynamic viscosity, $N.s.m^{-2}$
ρ	density, $kg.m^{-3}$
σ	Stefan–Boltzmann constant, 5.67 $W.m^{-2}.K^{-4}$

subscripts

b	bulk material property
C	cold side
con	combined solid and gas conduction
g	gas conduction
$g0$	gas conduction at atmospheric pressure
H	hot side
i	various depths inside insulation
int	integrated
LP	low pressure
r	radiation
s	solid conduction
T	test sample

1. Introduction

Heat transfer in a high-porosity fibrous insulation is composed of combined radiation and conduction heat transfer, with conduction consisting of both solid and gaseous conduction modes. Fibrous insulation materials typically have low solid conduction due to their high porosity, typically 95% or higher. The fibers scatter and absorb impinging radiation, while emitting their own radiation. Because of small pore size in insulation materials, the gas conduction mode of heat transfer at low and intermediate static pressures is attenuated. The attenuation is due to gas mean free path at low pressures being significantly larger than the typical pore size. Solid conduction is a significant mode of heat transfer in rigid (bonded) insulation samples. Solid conduction is less significant in flexible (unbonded) insulation samples compared to rigid samples, with solid conduction's relative significance increasing with increasing density and generally decreasing with increasing temperature. The significance of radiation heat transfer increases with increasing temperature, and decreases with increasing insulation density. Gas conduction is negligible in vacuum and increases with increasing temperature and static pressure (at intermediate static pressures).

Semi-empirical approaches have traditionally been used for modeling of solid conduction in fibrous insulation (Refs. 1-3), because precise modeling of conduction through the fibers and fiber interfaces is almost impossible. The modeling of gas conduction in fibrous insulation is well established (Refs. 4-6). Modeling of radiation heat transfer through fibrous insulation is more complicated and has been the subject of numerous studies, with a comprehensive review of various radiation models provided elsewhere (Ref. 3). Significant work has been devoted to developing physics-based heat transfer modeling for rigid and flexible fibrous insulation with various degrees of complexity. The simplest approach has been the semi-empirical methods that use a combined radiation and conduction heat transfer model with radiation conductivity in terms of a Rosseland mean coefficient based on the diffusion approximation (Ref. 7). The semi-empirical techniques infer radiative thermal conductivity or total radiative extinction coefficient from

experimental data. Later models used more refined radiation models based on scattering intensity distribution from infinite cylinders from the solution of Maxwell's equations (Refs. 8, 9). Houston and Korpela (Ref. 10) and Lee (Refs. 11, 12) developed a rigorous formulation for scattering properties of fibrous insulation that accounted for the two-dimensional scattering characteristics of fibers, with the resulting radiation model using deterministic parameters that define the composition and morphology of the medium: fiber size distribution, fiber orientation, fiber volume fraction, and the spectral complex refractive index of the fibers. The rigorous predictive formulation of Lee is complicated and has so far been applied to Space Shuttle tiles (Ref. 3), a carbon felt (Ref. 13), a fumed silica standard reference material from the National Institute of Standards and Technology (Ref. 14), and a flexible alumina-based insulation felt (Ref. 15).

The semi-empirical thermal model that was previously used by the author to model various insulation materials for temperatures between 300 K and 1400 K (Ref. 6) is further refined here and applied to five insulation samples between 300 K and 1900 K. The model relies on a semi-empirical solid conduction component formulation, and radiation conductivity in terms of a Rosseland mean coefficient based on the diffusion approximation. The model uses the standard gas conduction component formulation (Ref. 4-6). Some of the parameters needed for the thermal model are inferred from thermal test data.

There is a need for a steady-state thermal test setup that can provide accurate thermal conductivity of high-temperature, high-porosity insulation materials over the static pressure range of 0.001 torr (0.13 Pa) to 760 torr (101.3 kPa), and temperature range of 300 K to 1900 K. The data from the test setup can then be used to infer parameters for the semi-empirical thermal model, or to validate thermal models of various degrees of complexity. The thermal conductivity of a high-porosity insulation is a function of temperature, static pressure, insulation density, thermal and radiative properties of insulation material, and the gaseous medium filling the insulation (Ref. 6). Various standard steady-state techniques (Refs. 16-18) can be utilized for measuring the thermal conductivity of high-porosity thermal insulation samples. The guarded-hot-plate technique (Ref. 16) is the most accurate technique for testing of insulation samples but requires significant setup and test time to achieve steady-state conditions in order to yield accurate results. Ensuring one-dimensional heat transfer through the sample and balancing the main and guard heaters in the system can take 20 to 30 hours per data point to generate accurate data (Ref. 13). Some guarded-hot-plate test setups can operate up to 1200 K (Ref. 13), but most of the test setups have upper temperature limits in the range of 600 K to 900 K (Refs. 19-20). The heat flow meter technique (Ref. 17) can yield accurate results with a faster turnaround time compared to the guarded-hot-plate technique and has been previously used to measure thermal conductivity of various insulation samples up to 1400 K (Ref. 6). Both guarded-hot-plate and heat flow meter techniques can provide thermal conductivity as a function of temperature and static pressure. The radial flow technique (Ref. 18) can also be used for measuring thermal conductivity of insulation samples, but the high-temperature version of the apparatus available in the United States is limited to testing at atmospheric pressure for temperatures above 1000 K (Ref. 20). The guarded-comparative-longitudinal heat flow technique (Ref. 21) is intended for homogenous opaque solids and is not suitable for testing of insulation materials, which are inherently semi-transparent to thermal radiation. Some transient techniques are also used for measuring the thermal diffusivity of high-porosity insulation materials. The most common transient technique is the laser flash method (Ref. 22) which is intended for opaque materials and is not suitable for high-porosity, semi-transparent insulation materials. The three-point step heating technique has been developed as an alternative to the laser flash technique to measure thermal diffusivity of high-porosity insulation materials up to 1100 K (Ref. 23) at various static pressures. The transient techniques measure thermal diffusivity and require the specific heat of the test sample to calculate thermal conductivity from the measured thermal diffusivity. Specific heat data can typically be obtained from the differential scanning calorimetry technique (Ref. 24). Another simple transient test technique operating at atmospheric pressure has been used in conjunction with inverse techniques to infer thermal properties of insulation materials and opaque materials with low thermal conductivity (Refs. 25, 26).

The heat flow meter (Ref. 17) test setup at NASA Langley Research Center (LaRC) was previously used for testing of flexible (unbonded) felts (Ref. 6) and rigid (bonded) insulation materials (Refs. 27, 28) up to 1400 K at pressures between 0.001 torr and 760 torr. The test setup has recently been upgraded to extend the upper temperature limit to 1900 K and is used in the present study to measure thermal conductivity of four samples and develop thermal models for the insulation samples.

The objective of the current work is to provide test data and corresponding thermal models on five insulation materials up to 1900 K. First the thermal model is presented. The test setup and experimental procedure are discussed including design considerations for ensuring one-dimensional heat transfer. Then, new low-pressure thermal conductivity experimental data on two flexible refractory ceramic felts up to 1700 K is provided and compared with previous data up to 1400 K (Ref. 6): an yttria-stabilized zirconia insulation and an alumina-based paper insulation. The data processing technique to obtain the low-pressure thermal conductivity is discussed. Thermal conductivity data at higher pressures are then generated using the standard gas conduction formulation (Refs. 4-6). A more detailed model for separating the low-pressure thermal conductivity data into its solid conduction and radiation components for these two insulation materials is also provided. Afterwards, thermal conductivity data and thermal models of two composite fibrous insulation samples are presented: an alumina-based insulation sample containing silicon carbide opacifiers for reducing radiation, and an alumina-based insulation sample containing aluminosilicate aerogels for reducing gas conduction. Then, data on a previously reported (Ref. 6) alumina-based insulation are re-processed using the updated data processing technique. Finally, the relative significance of various modes of heat transfer in a typical fibrous insulation is discussed and used to provide general guidance for optimum insulation layups for typical aerospace applications.

2. Thermal Model

The semi-empirical thermal model used in this study was previously used to analyze experimental data of various insulation materials up to 1400 K (Refs. 6, 28). In fibrous insulation with density of 20 kg.m^{-3} or higher, natural convection is insignificant (Refs. 29, 30). Forced convection in fibrous insulation is insignificant without the presence of a sufficient pressure gradient and flow path across the insulation. In the absence of forced and natural convention, conduction and radiation are the only modes of heat transfer in fibrous insulation. Conduction consists of both solid and gas conduction modes. A scanning electron microscopy (SEM) image of APA^{TM,}[1], an alumina paper insulation, with a magnification factor of 1500 is shown in Figure 1. Solid conduction occurs along the fibers and at the fiber-to-fiber contacts, while gas conduction takes place in the void space between the fibers. Radiation also occurs between the fibers, with the fibers scattering and absorbing incoming radiation, while emitting their own radiation.

Assuming one-dimensional heat transfer in the through-the-thickness direction of insulation, the steady-state energy conservation equation is (Ref. 31)

$$\frac{\partial}{\partial y}\left(k_{con}\frac{\partial T}{\partial y}\right) - \frac{\partial q_r''}{\partial y} = 0 \tag{1}$$

where k_{con} is the combined thermal conductivity due to both solid and gas conduction, q_r'' is the radiant heat flux, T is temperature, and y is the spatial coordinate in the through-the-thickness direction. The radiant heat flux is extremely complicated to model due to the integral nature of radiative transfer and the spectral and directional dependence of radiative properties. It is assumed the medium is optically thick, so that radiation can be modeled as a diffusion process, resulting in the radiant heat flux being approximated as (Ref. 31)

$$q_r'' = -k_r \frac{\partial T}{\partial y} \tag{2}$$

---

[1] Zircar Ceramics, Inc.

4
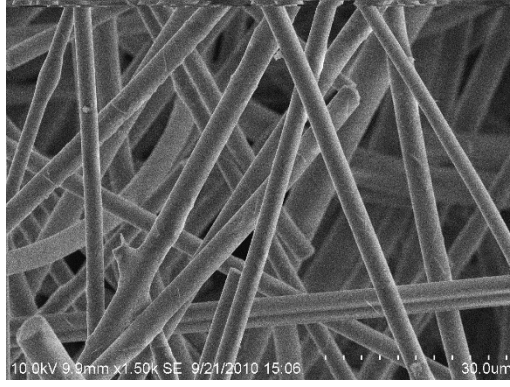
Figure 1. Scanning electron microscopy(SEM) image of alumina paper insulation.

with k_r representing a radiant conductivity. Using this approximation Eq. (1) reduces to

$$\frac{\partial}{\partial y}\left(k\frac{\partial T}{\partial y}\right) = 0 \tag{3}$$

where k is obtained by superposition of the thermal conductivities due to solid conduction, gas conduction, and radiation. Occasionally, k will be referred to as total thermal conductivity to distinguish it from its components

$$k = k_{con} + k_r = k_s + k_g + k_r \tag{4}$$

where k_{con} has been represented as the sum of solid thermal conductivity, k_s, and gas thermal conductivity, k_g. The simple superposition of solid and gas conduction thermal conductivities may underestimate the value of total thermal conductivity at higher pressures for some insulation samples (Ref. 32), because of potential gas-solid conduction coupling that is not addressed here.

An exact formulation for solid conduction in fibrous insulation is a formidable task because of the complicated nature of conduction through fibers of varying length and orientation, and conduction through fiber-to-fiber contacts (Ref. 3). A semi-empirical approach used by various other researchers (Refs. 1-3, 6) is used here to model solid conduction heat transfer in flexible fibrous insulation

$$k_s(T) = F\, f^m k_b(T) \tag{5}$$

which relates the solid thermal conductivity of fibrous insulation to the thermal conductivity of bulk fiber material, k_b, and fiber volume fraction, f, raised to a power m, typically between 1 and 3 (Refs. 1-3, 6, 30). The fiber volume fraction is the ratio of insulation test sample density, ρ_T, to the density of bulk fiber material, ρ_b

$$f = \frac{\rho_T}{\rho_b} \tag{6}$$

The thermal conductivity of bulk fiber material can be found in literature (Ref. 33). The parameter F is a scaling factor that relates the micro-scale geometric effects of the fiber matrix with bulk dimensions, and is assumed to be temperature independent (Ref. 3). A value of unity was used for the exponent m in Eq. (5) in the present study. The scaling parameter, F, can be obtained from cryogenic thermal conductivity measurements in vacuum, as will be discussed in proceeding sections.

The radiant thermal conductivity for fibrous insulation is provided by (Ref. 31)

$$k_r = \frac{16\,\sigma\, n^{*2}T^3}{3\rho_T\, e} \tag{7}$$

where σ is the Stefan Boltzmann constant. Specific extinction coefficient, e, is an intrinsic property of fibers and is a function of temperature, fiber optical properties, fiber diameter, and fiber orientation. The effective index of refraction of fibrous media, n^*, is typically a function of fiber optical properties, temperature, and

5

fiber volume fraction (Ref. 34). Both e and n^* are unknown and difficult to obtain unless the predictive modeling approach of Lee and Cunnington (Ref. 3) is utilized. In the present work, the combined quantity $e/n^{*2}(T)$ is estimated from experimental thermal conductivity data.

Gas thermal conductivity does not vary with pressure, but the exchange of heat from gas molecules to adjacent solid surfaces is influenced by the environmental pressure in the rarefied and transition transport regimes. Thus, an effective gas thermal conductivity can be defined as (Ref. 4-6)

$$k_g(T, P) = \frac{k_{g0}(T)}{1 + 2\frac{\beta}{Pr}Kn} \tag{8}$$

where $k_{g0}(T)$ is the thermal conductivity of the gas at atmospheric pressure, Pr is the Prandtl number, and Kn is the Knutson number. The parameter β is defined as

$$\beta = (\frac{2-\alpha}{\alpha})\frac{2\gamma}{(\gamma+1)} \tag{9}$$

where α is the thermal accommodation coefficient and γ is specific heat ratio. Since there is limited data for thermal accommodation coefficient between various gases and fiber materials, a thermal accommodation coefficient of unity was used for the fibrous insulation materials considered in the present study. The use of an accommodation coefficient of unity previously produced better agreement with experimental results in nitrogen gas (Refs. 6, 30). The Prandtl number is given by

$$\text{Pr} = \frac{\mu c_p}{k_{go}} \tag{10}$$

where μ is the viscosity, and c_p is the specific heat of the gas. The Knudsen number is defined as

$$Kn = \frac{\lambda}{\kappa} \tag{11}$$

where λ is the gas mean free path and κ is the gas conduction characteristic length or pore size. The gas mean free path is given by

$$\lambda = \frac{K_B T}{\sqrt{2}\pi d^2 P} \tag{12}$$

where K_B is the Boltzmann constant, P is pressure, and d is the gas collision diameter. The quantities $k_{go}(T)$, $\mu(T)$, $c_p(T)$ and d_m can be found in the literature for any gas (Refs. 35-38) and $Pr(T)$ and $\gamma(T)$ can then be calculated from these properties. The gas conduction contribution in fibrous insulation can be easily calculated if the gas conduction characteristic length (pore size) is known. The pore size, κ, for typical fibrous insulation samples is obtained from (Ref. 39)

$$\kappa = \frac{\pi}{4}\frac{D}{f} \tag{13}$$

where D is the average fiber diameter. For composite insulation samples that contain additives for attenuating either the radiation or gas conduction modes of heat transfer, this formula is not applicable, and the pore size must be estimated from experimental data.

In vacuum, where gas conduction in fibrous insulation material is insignificant, the low-pressure thermal conductivity, k_{LP}, which is the sum of radiant and solid thermal conductivity, can be directly obtained from experimental data

$$k_{LP} = k_s + k_r \tag{14}$$

Knowledge of $k_{LP}(T)$ from the experimental data and the gas conduction pore size, κ, is sufficient to calculate thermal conductivity data at various pressures and temperatures in various gases for the insulation at the specific density of the test sample. This modeling technique will be referred to as standard modeling, while separating k_{LP} to its constituents (radiation and solid conduction) and estimating F and e/n^{*2} from experimental data will be referred to as detailed modeling in this report. Using the detailed modeling one

can generate thermal conductivity data at various pressures and temperatures in various gases for various insulation densities, if the fiber insulation morphology does not change with density.

3. Test Setup and Instrumentation

A brief description of the test setup is provided. The test setup is located inside the 1.5 m (5 ft) vacuum chamber in Building 1250 at LaRC. The chamber diameter and depth are 1.5 m each. Chamber pressure can typically be lowered to 10^{-5} torr using a cryogenic vacuum pump. For testing of insulation samples, a pressure of 10^{-3} torr is sufficient to ensure effective absence of gas conduction heat transfer in the test sample. The chamber is typically backfilled with nitrogen gas to increase the pressure. Other gases, such as carbon dioxide and argon, have been used to backfill the chamber for some tests (Ref. 28). Backfilling with atmospheric air is not recommended when testing at elevated temperature due to possible oxidation of the test setup components. A schematic of the overall test setup is shown in Figure 2. The main components of the test setup are a graphite heater, a graphite septum plate, an insulation test sample, and a water-cooled plate. A water-cooled copper picture frame is installed around the water-cooled plate with surrounding insulation and refractory ceramic insulation boards placed above to minimize heat losses to the chamber, as shown in the figure. The test sample is sandwiched between the graphite septum plate and the water-cooled plate. The septum plate is heated directly by the graphite heater and serves as the hot boundary of the test sample. The earlier version of the system used quartz lamps heaters with an Inconel septum plate, with maximum septum plate test temperature of 1400 K. The use of a graphite heater and graphite septum plate has increased the maximum test temperature to 1900 K.
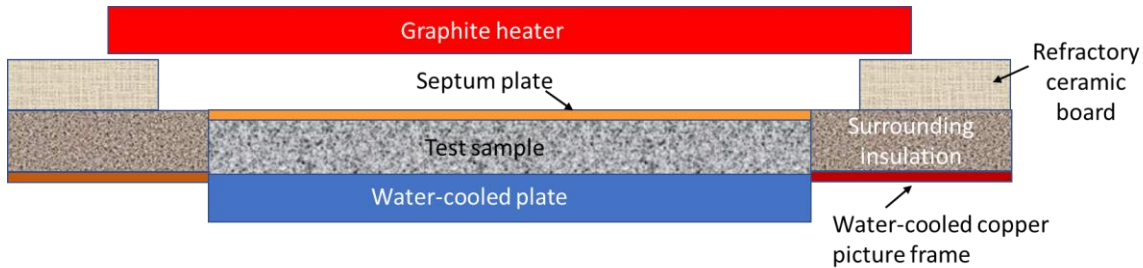
Figure 2. Schematic of test setup.

The main feature of the test setup is that the sample dimensions enable one-dimensional (1-D) or quasi 1-D heat transfer in the test sample. The test set up dimensions were selected to ensure the thermal resistance in the through-the-thickness (TTT) direction of the test sample is significantly lower than the thermal resistance in the in-plane (IP) direction since heat follows the path of least thermal resistance. The test samples have planar dimensions of 305 mm × 305 mm, while the typical test sample thickness can vary between 13 mm and 51 mm. The preferred test sample thickness is 25.4 mm or less, providing a thickness to planar dimension ratio of 0.083. As a rule of thumb, a thickness to planar dimension ratio of 0.1 or lower ensures 1-D heat transfer in the central section of the test sample (central 152 mm x 152 mm section) and minimizes edge effects as will be seen in proceeding thermal resistance calculations. This discussion is valid for thermal conductivity testing of any material, and not just high-porosity thermal insulation material.

Thermal resistance, R, is defined as

$$R = \frac{L}{k\,A} \tag{15}$$

where L is the distance heat has to travel, A is the cross-sectional area for transfer of heat, and k is thermal conductivity. For a test sample with thickness of 0.0254 m and cross-sectional area of 0.093 m^2 (0.305 m × 0.305 m) the TTT thermal resistance is

$$R_{TTT} = \frac{0.0254}{0.093 \, k_{TTT}} = \frac{0.273}{k_{TTT}} \tag{16.a}$$

The IP thermal resistance for transfer of heat from the center of the test sample to the edges of the test sample is

$$R_{IP} = \frac{0.1525}{4(0.0254 \times 0.1525) \, k_{IP}} = \frac{9.842}{k_{IP}} \tag{16.b}$$

The distance from the center to the edge of the sample is 0.1525 m, while the in-plane cross sectional area consists of 4 surfaces with dimensions of 0.0254 m × 0.1525 m. Assuming the test sample has an isotropic thermal conductivity ($k_{IP} = k_{TTT}$), the ratio of IP to TTT thermal resistance is

$$\frac{R_{IP}}{R_{TTT}} = \frac{9.842}{0.273} = 36 \tag{17}$$

The high resistance ratio ensures that most of the heat will be transferred in the TTT direction with its significantly lower thermal resistance. A ratio larger than 10 is desirable. If the IP thermal conductivity is higher than the TTT thermal conductivity, then the ratio drops below 36. The choice of sample dimensions can affect the ratio of IP to TTT thermal resistances, which can dictate whether heat transfer is one-dimensional or multi-dimensional. Using a sample thickness 0.0508 m in this test setup will result in the IP to TTT thermal resistance ratio of 9, which may or may not result in one dimensional heat transfer depending on TTT and IP temperature gradients. The large IP thermal resistance also minimize edge effects on heat transfer in the central section of the test setup.

The various components of the test setup are briefly described. The water-cooled plate is a 25.4-mm thick aluminum plate, with planar dimensions of 305 mm × 305 mm, with nine cylindrical cooling channels drilled through the plate. Nine thin heat flux gauges, thermopiles encapsulated in polyimide film, 0.15-mm thick were installed on the water-cooled plate. A 0.13-mm thick polyimide sheet covered the plate at locations not covered by the heat flux gauges. The heat flux gauges and polyimide sheet were bonded to the water-cooled plate using a vacuum bag epoxy technique, and then painted with a flat black paint with an emittance of 0.9. A photograph of the water-cooled plate prior to being painted is shown in Figure 3.a, where the nine heat flux gauges and trenches for routing of the associated lead wires are visible. A schematic drawing showing the heat flux gauge locations on the water-cooled plate is provided in Figure 3.b. The manufacturer-supplied calibration data for the heat flux gauges[2] is used to covert measured voltage to heat flux. The manufacturer calibration had previously been verified on select gauges by radiant tests of the heat flux gauges subject to a high intensity irradiance standard (Ref. 40). Each heat flux gauge also contains a type T thermocouple for measuring the gauge temperature, which is used for temperature correction of the measured voltage. The average heat flux and temperature calculated from the five heat flux gauges located in the central region of the water-cooled plate, referred to as the metered region, provide the average heat flux, q'', and average test setup cold-side temperature, T_C. A photograph of the water-cooled plate during assembly in the test setup is shown in Figure 4. The water-cooled plate is located on a 305 mm × 305 mm × 25.4-mm thick Bakelite plate which is installed on laboratory jacks with adjustable heights. The water-cooled plate is surrounded by a 101-mm wide water-cooled copper picture frame, which is a new feature of the test setup. Graphite felt picture-frame insulation is installed on top of the copper picture frame to minimize heat losses/gains from the sides of the test sample, as seen in Figure 5. The height of the graphite felt picture frame is adjusted during test sample assembly to match the height of the test sample. By using the water-cooled copper picture frame, the graphite felt insulation picture frame surrounding the test sample has a cold-side boundary condition similar to the test sample: both have water-cooled boundaries.

---

[2] RDF Corp.

a)   b)
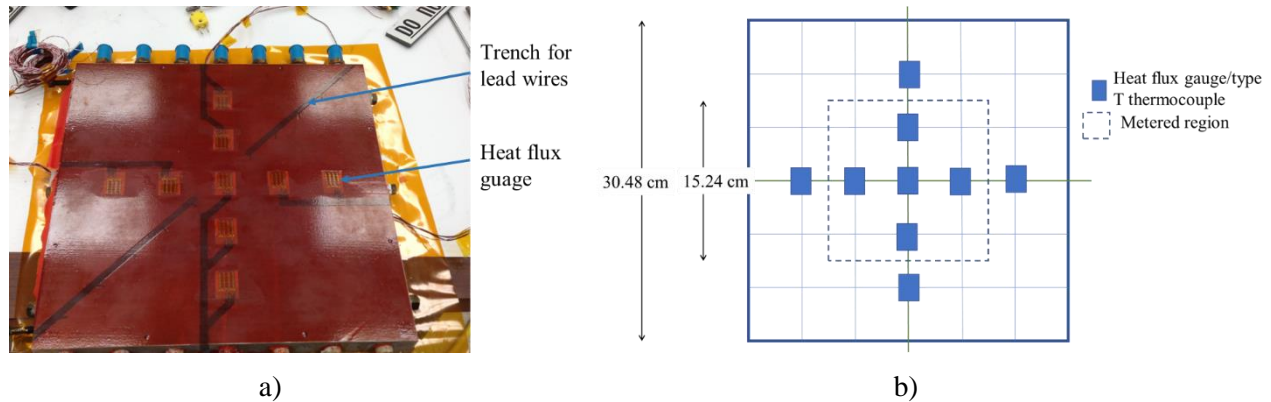
Figure 3. Water-cooled plate: a) photograph of water-cooled plate prior to surface being painted with black paint, b) schematic of heat flux gauge layout.
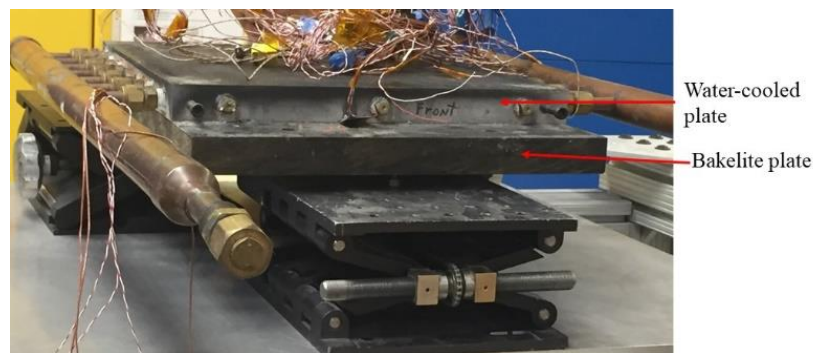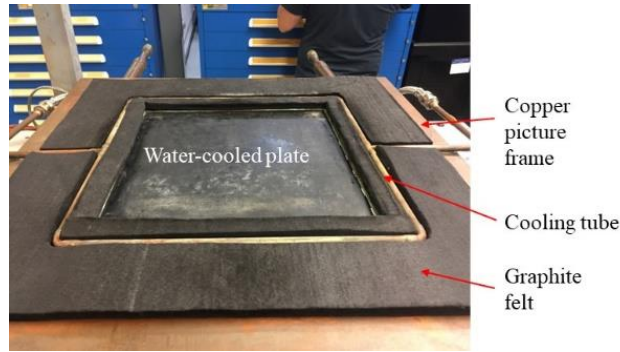

Figure 4. Photograph of water-cooled plate in test setup.

A photograph of a test sample and the surrounding graphite felt insulation installed in the test setup is shown in Figure 6. A type K thermocouple laid on top of the test sample is seen in the figure. A portion of the lead wires (from thermocouple junction to the edge of the test sample) are bare and the rest covered in Nextel sleeving.[3] Thermocouples for use at various depths inside the sample will be discussed in the proceeding discussion.

The septum plate is then installed on top of the test sample to provide the hot-side boundary condition. The septum plate is a 6.4-mm thick graphite plate with planar dimensions of 305 mm × 305 mm, and typically instrumented with four to six 0.508-mm diameter type C thermocouples. A schematic drawing of the thermocouple locations on the septum plate for a four-thermocouple installation, and the corresponding photograph of the plate are shown in Figure 7. Type C thermocouples are used because they could operate at 1900 K and were more durable than noble-type thermocouples (using various platinum alloys) for the present test setup. For these thermocouples, bare wires are used with 25.4-mm length of the lead wires adjacent to the thermocouple junction flame sprayed with alumina to avoid electrical shorting with each other and the septum plate. The remainder of the lead wires are covered with Nextel sleeving.

A trench of sufficient depth/width is incorporated in the graphite septum plate for routing of each thermocouple. A high-temperature ceramic adhesive was used to hold the thermocouple lead wires in place at the junction location and at the septum plate edge, as seen Figure 7. The thermocouple side of the graphite plate is placed on top of the sample, with the flush-mounted thermocouples providing the temperature at the septum plate/test sample interface. The temperature on the graphite plate is spatially

---

[3] 3M Company

9

**Figure 5. Photograph of water-cooled plate and water-cooled copper picture frame.**
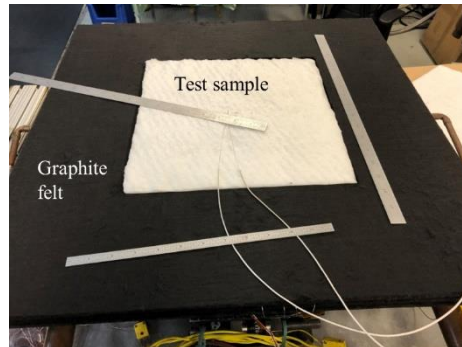
Figure 6. Photograph of test sample and graphite felt picture frame insulation installed in test setup.

uniform due to the high thermal conductivity of graphite, therefore, four thermocouples were deemed sufficient to obtain the average temperature of the central metered region of the septum plate as the hot-side temperature, T_H. A photograph of the septum plate installed on the test sample in the test setup is shown in Figure 8. Carbon-carbon sheet strips, 51-mm wide, approximately 305-mm long are placed on top of the septum plate/surrounding graphite felt insulation interfaces to minimize any possible radiation shine-through from the radiant heater to test sample due to presence of any potential gaps. Even though gaps are sometimes used in low-temperature thermal conductivity test setups to thermally isolate parts (sample from surrounding material), they should be avoided in high-temperature testing, where radiation shine-through in gaps can be significant and can alter the thermal response of test sample in an unaccounted fashion.

SALI™ board refractory ceramic board[4] pieces, 76-mm wide × 12.5-mm thick, are then placed on top of the graphite felt insulation picture frame, around the outer edges of the picture frame, to form a 25-mm to 51-mm high rigid enclosure to minimize radiation loss from the graphite heater to the chamber as depicted in Figure 2. After assembly, the test setup is placed in the vacuum chamber such that it is directly below the graphite heater assembly. The height of test assembly is adjusted using the jacks located below the water-cooled plate to leave a minimum gap between test setup and heater. The graphite heating system operates on high current (up to 500 amps) and low voltage. Previously, a quartz lamp array heater was used as the heater for the setup, which operated at 60 amps and maximum voltage of 208 volts to prevent corona discharge and arcing in the chamber that could potentially occur at higher voltages and at some pressures, limiting the maximum sample hot-side temperature to 1400 K. The new graphite heating system enables testing with sample hot-side temperature up to 1900 K, but typically the maximum operating temperature is limited to 1800 K for maintaining durability of some test setup components. A photograph of the test setup in the vacuum chamber is shown in Figure 9.
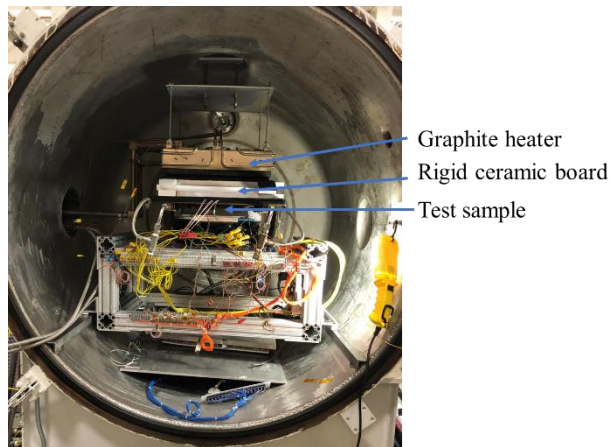
---

[4] Zircar Ceramics, Inc.

a)   b)
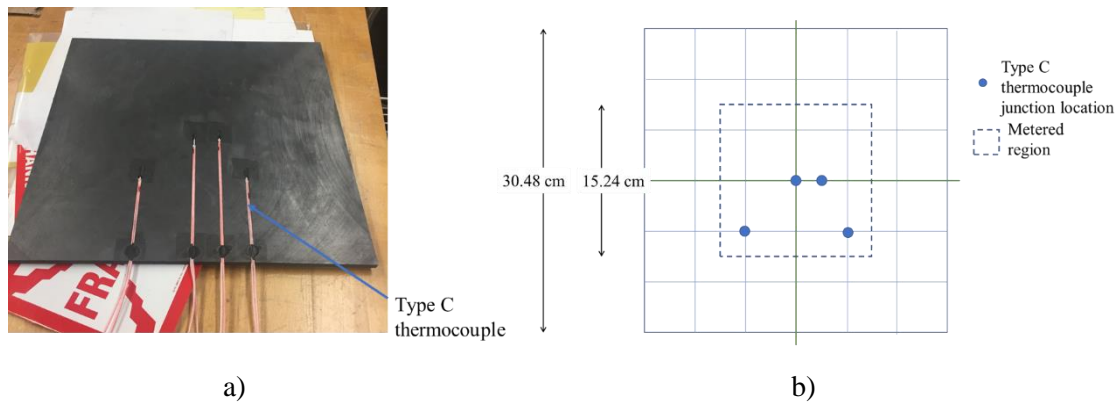
Figure 7. Septum plate: a) photograph of septum plate with type C thermocouples, b) schematic of thermocouple layout.
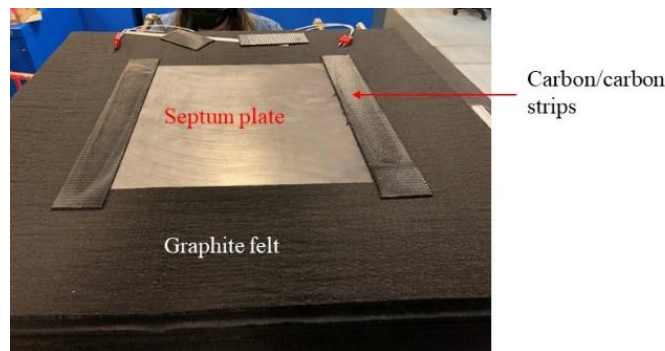

Figure 8. Photograph of septum plate installed in test setup.

Figure 9. Photograph of test setup in the vacuum chamber.

If possible, the sample is instrumented with internal thermocouples to measure the sample temperature at various depths throughout the sample thickness. Since the sample is typically exposed to large temperature gradients across its thickness during the test (T_C typically maintained at room temperature, while T_H varies between 500 K and 1900 K), measuring temperature at various locations through the sample thickness provides additional data for data processing. Three to five thermocouples are typically used for this purpose in a 25.4-mm thick sample, as shown schematically in Figure 10, with T_i representing temperature measured

11

at height L_i, measured from the water-cooled plate. Installation of internal thermocouples is more easily achieved for thin felts where multiple felt layers are stacked to achieve the desired 25.4-mm test sample thickness. The thermocouples are then installed at the interfaces of various layers. For instance, LaRC Test 602 for APA used 21 stacked layers to achieve the desired thickness. Thermocouples were installed on top of the fifth, tenth, and fifteenth layer of APA measured from the water-cooled plate. The thermocouple used
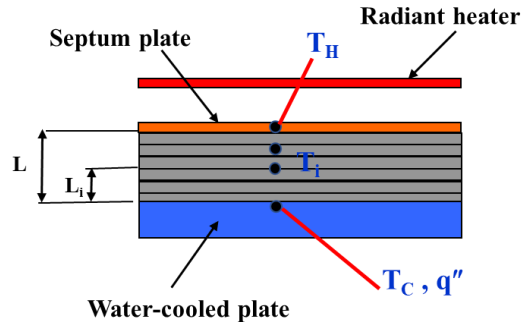
**Figure 10. Schematic of test setup and instrumentation.**

is either type K, for in-depth locations closer to the water-cooled plate, or type C for in-depth locations closer to the septum plate for tests where septum plate temperature exceeds 1400 K. For type K thermocouples, typically metal-sheathed thermocouples with overall diameter of either 0.254 mm or 0.508 mm are used. The thermocouple wires and surrounding ceramic spacers are all located within a high-temperature alloy outer sheath with the overall outer diameter provided above. A photograph of metal sheathed thermocouples installed on top of an insulation test sample that had been encased in fabric and quilted is shown in Figure 11. Another option is to use bare (uninsulated) type K or type C thermocouples with typical lead wire diameter of 0.254 mm. The length of the thermocouple inside the test sample is bare to minimize thermal disturbance of the test sample environment. Care is taken to ensure the two bare lead wires are sufficiently distanced from each other, from the thermocouple junction location to the edge of the sample, to prevent potential touching of leads that could change the effective thermocouple junction location. Nextel sleeving is placed around each lead wire from the test sample edge for the rest of thermocouple length, as shown in Figure 6. In some cases, in-house manufactured type K foil thermocouples are used. In this case, the two bare lead wires are spot welded to the edges of a thin Inconel foil as shown in Figure 12. The thin foil serves as the effective thermocouple junction, with a larger overall surface area compared to a typical thermocouple welded bead, which can potentially provide more accurate data in radiation dominated environments at high temperatures in vacuum. The sample in-depth thermocouples are typically placed so that the thermocouple junctions are located within a 51-mm wide region around the center of sample, and staggered throughout so that not all junctions are at the same planar location: for example, one junction is placed in the center, one junction is 51 mm to the right of center, and one 25 mm to the left of the center. This staggering of thermocouple junction locations is intended to minimize disturbances of the thermal/radiative environments.

Three types of calibrated pressure gauges are used to ensure continuous pressure measurements over the range of high vacuum to atmospheric pressure. A capacitance gauge is used between atmospheric pressure and 10 torr. A Pirani gauge is used between 10 torr and 5×10^{-3} torr, and an ionization gauge is used below 5×10^{-3} torr. The crossover between these gauges is automatic.
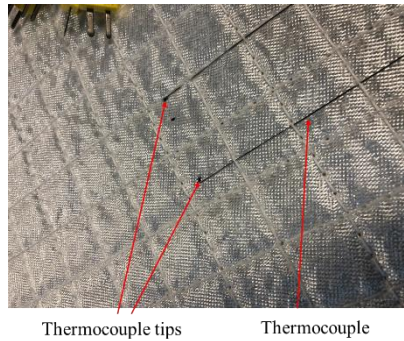
Figure 11. Metal sheathed thermocouples installed on a quilted test sample.
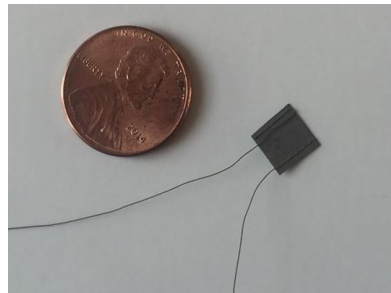
Figure 12. A thin foil thermocouple.

4. Test Procedure

The test sample is typically heat treated in an oven to remove any binders and impurities present in the sample before testing in the vacuum chamber. The heat treatment prevents excessive outgassing of the sample at low pressures and at moderate to high temperatures that could potentially contaminate the cryogenic vacuum pump. Sample dimensions and mass are then measured to determine sample density and thickness. Sample is placed in the test setup outside of the vacuum chamber. If necessary, the sample is instrumented with internal thermocouples to measure the temperature at various depths throughout sample thickness. The test setup is then placed in the vacuum chamber and the instrumentation is connected to respective terminals.

The vacuum chamber is evacuated and maintained at low pressures to ensure sufficient removal of moisture and various gases from the chamber. The vacuum chamber pressure is then set at 10^{-3} torr, and the septum plate is heated to the lowest setpoint temperature, typically 500 K. During the initial heating some outgassing of test sample and test setup components may occur, which can be observed by chamber pressure fluctuations. Once outgassing is completed, the chamber pressure is stabilized at 10^{-3} torr. The internal sample temperatures, T_i, and the average heat flux gauge data in the metered region, q'', are monitored to determine when the test setup has reached steady-state conditions. It is essential to use test data for calculation of thermal conductivity only after steady-state conditions have been achieved. Then the septum plate temperature is raised to the next setpoint. Typically, seven septum plate setpoint temperatures at 10^{-3} torr pressure are used to determine the low-pressure thermal conductivity, k_{LP}, of the test sample over the desired temperature range. The highest setpoint is the highest intended use temperature for the insulation being tested, with the highest possible setpoint being 1900 K in the current setup. If no internal sample thermocouples are used, it is recommended to use seven or more septum plate setpoint temperatures. Use of internal sample thermocouples provides additional temperature data at each septum plate setpoint, thus potentially allowing for a reduction in the number of setpoint temperatures without loss of accuracy. Once

13

k_{LP} is determined, the combined contributions of solid conduction and radiation modes of heat transfer in the insulation test sample is known, Eq. (14). Gas conduction is the only other heat transfer mode to be determined to fully characterize the thermal performance of the test sample, with the only unknown being the insulation pore size. Eq. (13) can be used to calculate the pore size in typical fibrous insulation samples. For more complex insulation samples that have additives for reducing either the gas conduction or radiation modes of heat transfer, the pore size needs to be determined experimentally. To determine or verify the pore size, a pressure scan at one septum plate temperature is needed. The septum plate is set at one temperature in vacuum and data is taken at steady-state conditions. The pressure is then increased to the next pressure setpoint, while the chamber is backfilled with nitrogen gas, and data is taken at steady-state conditions. This process must be repeated for seven to ten pressure setpoints between 10^{-3} torr and 760 torr. For typical fibrous insulation material, the overall thermal conductivity is not very sensitive to pressure in two pressure ranges: between 10^{-3} torr and 0.1 torr (rarefied gas conduction regime) and between 100 torr and 760 torr (continuum gas conduction regime). The highest sensitivity is found between 0.1 torr and 100 torr, so it is better to have more pressure setpoints in this range (transition region for gas conduction).

5. Data Processing

At each hot-side setpoint temperature, the average heat flux, q'', average water-cooled plate temperature, T_C, average septum plate temperature, T_H, and internal sample temperatures, T_i, are collected once steady-state conditions have been achieved. The measured heat flux and temperature data are then used to calculate thermal conductivity. Most thermal conductivity measurement systems impose a small temperature difference (typically 1 K to 5 K) across the sample thickness at the test temperature to infer thermal conductivity at the average local temperature. The present system imposes large temperature differences (200 K to 1600 K) across the sample thickness, so it does not directly provide thermal conductivity measurements. Instead, it provides a quantity that is the thermal conductivity integrated over a large temperature difference, and then the actual thermal conductivity must be inferred from this integrated value. The details will be provided here. Referring to Figure 10, for each internal thermocouple temperature and the hot-side temperature, an integrated thermal conductivity is calculated using

$$k_{int} = \frac{L_i \, q''}{T_i - T_C} \tag{18}$$

where T_i represents any of the measured internal temperatures T_1, T_2, T_3, and septum plate temperature, T_H, while L_i represents the corresponding distance between these thermocouples and the water-cooled plate. For instance, for three in-depth thermocouples, at any septum plate setpoint temperature four integrated thermal conductivities are calculated. Testing at seven setpoint temperatures results in 28 integrated thermal conductivity data points. In previous publications k_{int} was referred to as "effective thermal conductivity," which could be misleading, because the calculated k_{int} *is a function of T_i, T_c, and P [k_{int} (T_i, T_c, P)]*, which is different from thermal conductivity, which is a function of local temperature and pressure, $k(T,P)$. k_{int} is related to k through

$$k_{int}(T_i, T_C, P) = \frac{1}{T_i - T_C} \int_{T_C}^{T_i} k(T, P) \, dT \tag{19}$$

where k_{int} is the integral of k with respect to temperature with the lower integration limit set to T_C, and the upper integration limit set to various T_i (T_1, T_2, T_3, … ,T_H). If the measurements are conducted in vacuum (0.001 torr) then the thermal conductivity term in the integrand on the right-hand side of Eq. (19) is the low-pressure thermal conductivity, k_{LP}.

It is typically assumed that k_{LP} varies with temperature using a third order polynomial (because radiant flux is a function of T^4)

$$k_{LP} = k(T, 0.001 \text{ torr}) = \sum_{i=0}^{3} a_i T^i \tag{20}$$

Substituting Eq. (20) for k in Eq. (19) and performing the integration leads to

$$k_{int}(T_i, T_C, 0.001) \ = \ a_0 + 0.5a_1(T_i + T_c) + \frac{a_2}{3}\left(T_i^2 + T_i T_C + T_C^2\right) + \frac{a_3}{4}(T_i + T_c)\left(T_i^2 + T_C^2\right) \ (21)$$

The four unknown coefficients, a_i, need to be calculated. For the example provided above for a sample with three internal thermocouples tested at seven setpoint temperatures in vacuum, there are 28 sets of data for k_{int}, T_i, T_c. A regression analysis is used to find the least-square fit for the unknown coefficients, a_i. Once, a_i are known, k_{LP} is known according to Eq. (20). Then if the gas conduction pore size is known, thermal conductivity data at higher pressures can be calculated using Eqs. (8-12, 4). If the pore size is unknown, it can be estimated from measured k_{int} at various pressures at a constant T_H using an equal search interval optimization routine. For various estimates of κ, k_g is calculated from Eq. (8), added to k_{LP} from Eq. (20), then integrated using Eq. (19) for each of the corresponding sets of input data (T_i, T_c, P) to estimate k_{int}. A value of κ is sought that would minimize the root sum square difference between the estimated and measured k_{int} values. Once κ is determined from test data in one gas, gas thermal conductivity data can be calculated for any gas, if the relevant gas properties needed in Eqs. (8 -12) are known (Refs. 35-38).

6. Test Samples

Data for five flexible insulation samples are presented. The first sample is yttria-stabilized zirconia (ZYF[TM]) felt,[5] which is rated for operation up to 2300 K. According to the manufacturer, it is a needled felt comprised of fibers having diameters between 4 μm and 6 μm, containing by weight 89% zirconia, 10% yttria, and 1% other oxides. The manufacturer-specified nominal felt thickness is 2.54 mm, with a nominal density of 240 kg.m^{-3}, and a nominal porosity of 96%. Thermal conductivity data were generated (LaRC Test 601) on a sample consisting of 11 felt layers, with a total sample thickness of 25.4 mm, yielding an effective layer thickness of 2.31 mm, and a calculated pre-test sample density of 289 kg.m^{-3} (for a 305 mm × 305 mm × 25.4 mm sample). The post-test sample density was 288.4 kg.m^{-3}. The ZYF sample had three internal thermocouples located on top of the second, fifth, and eighth layers from the water-cooled plate resulting in non-dimensional heights with respect to sample thickness (L_i/L) of 0.182, 0.454, and 0.727. The low-pressure thermal conductivity data were generated up to 1700 K, and results were compared to previously generated data from LaRC Test 540 that had been tested up to 1400 K (Ref. 6). Test 540 sample was also 25.4-mm thick, consisting of 11 layers of insulation with thermocouples located on top of the first, third, fifth, and seventh layers. The calculated sample density for Test 540 was 270.8 kg.m^{-3}. The detailed modeling was applied to Test 601 data to develop models for the solid conduction and radiation modes of heat transfer in ZYF.

The second sample is alumina paper (APA) felt, which is rated for operation up to 1950 K. The sample, designated by the manufacturer as APA-2 was tested (LaRC Test 602) up to 1700 K. According to the manufacturer, the sample contains by weight 86% alumina, 10% silica, and 4% other oxides, with a nominal felt thickness of 1.04 mm and nominal density of 120 kg.m^{-3}. Test 602 sample consisted of 21 felt layers, with a total sample thickness of 25.4 mm, yielding an effective layer thickness of 1.21 mm and a calculated pre-test sample density of 98.4 kg.m^{-3} (for a 305 mm × 305 mm × 25.4 mm sample), and a post-test sample density of 97.2 kg.m^{-3}. The calculated pre-test density of the 21-layer is lower than the manufacturer-specified density. Some of the discrepancy may be due to the variations of actual sample densities from the nominal values. Also, stacking 21 layers may not result in a total thickness equal to 21 times the nominal layer thickness, because of lack of perfect mechanical contact between layers. The calculated density of the test sample (98.4 kg.m^{-3}) is used for the calculations. The APA sample had three internal thermocouples located on top of the fifth, tenth, and fifteenth layers from the water-cooled plate resulting in non-dimensional heights with respect to sample thickness (L_i/L) of 0.238, 0.476, and 0.714. The generated low-pressure thermal conductivity data were compared to previous data from LaRC Tests 541 and 544 that had

---

[5] Zircar Zirconia, Inc.

been tested up to 1400 K (Ref. 6). Both Test 541 and 544 samples consisted of 23 layers of APA-1 with a total thickness of 25.4 mm, with calculated densities of 107 kg.m^{-3} and 108 kg.m^{-3} for Tests 541 and 544, respectively. APA-1 has a nominal density of 125 kg.m^{-3} and a nominal thickness of 1 mm according to the manufacturer. APA-1 has 9% organic binder, which had been burned off by heat treatment before the tests. The resulting composition of APA-1 after binder burn-off is supposed to match the APA-2 composition. Test 544 sample had four internal thermocouples located on top of the fifth, tenth, fifteenth, and twentieth layers, resulting in non-dimensional heights (L_i/L) of 0.217, 0.435, 0.652, and 0.869. Test 541 sample had no internal thermocouples. The detailed modeling was applied to Test 602 data to develop models for the solid conduction and radiation modes of heat transfer in APA.

The third sample is opacified fibrous insulation (OFI) which consists of silicon carbide opacifiers embedded in an alumina-based fibrous insulation sample. Silicon carbide is very effective in scattering of radiation (Ref. 41), thus reducing the radiation component of heat transfer in fibrous insulation samples. OFI samples can be produced by embedding opacifiers in various fibrous insulation samples, and the ratio of base fiber to opacifier mass can be tailored to provide an optimized insulation for the specific application. The first use of opacifiers was by Grunert, et al. (Ref. 42) who used dispersion of metallic particles or flakes (copper, aluminum, or nickel) in glass and quartz fiber matrix in multilayer insulation samples, and evaluated the thermal performance of samples up to 1200 K in vacuum. Various oxides and carbides are used as opacifiers, with titanium dioxide being the most commonly used opacifier. The specific OFI[6] discussed in the present study (LaRC Test 603) was manufactured by embedding silicon carbide opacifiers in an alumina fiber matrix and had a total pre-test density of 99.2 kg.m^{-3}. The test sample consisted of seven layers of OFI with a total thickness of 27.69 mm. The test sample was instrumented with four internal thermocouples, with non-dimensional heights (L_i/L) of 0.143, 0.286, 0.571, and 0.857. The post-test sample density was 97.5 kg.m^{-3}. Thermal conductivity data from the OFI sample are compared to APA to evaluate the effectiveness of opacifiers in radiation heat transfer attenuation.

The fourth sample was intended to evaluate insulation material that inhibit gas conduction. Microporous insulation materials, such as Min-K[TM,7] which is composed of fumed silica, are the first generation of gas conduction attenuating insulation samples. Microporous insulations are fragile and usually require encasement in high-temperature fabric and quilting. Aerogels are also very effective in reducing the gas conduction mode of heat transfer because of their small pore size. Aerogels are fragile and transparent to radiation heat transfer, therefore, more recent attempts for manufacturing of aerogel-based insulation samples for aerospace applications has concentrated on embedding aerogels in a fibrous insulation matt as the backbone structure. The fibers also help with scattering and absorption of radiation, thus making the composite sample less transparent. Silica aerogel is the most common type of aerogel used, but its use is limited to 900 K, while aluminosilicate aerogels can operate up to 1400 K. The fourth sample presented here consists of APA-2 felt with embedded aluminosilicate aerogel, manufactured by NASA Glenn Research Center and designated as APA2-AS (Ref. 43). The various aerogel manufacturing phases are carried out on an APA-2 felt. Twenty layers of APA2-AS were used to get a sample thickness of 24.61 mm. The sample density (LaRC Test 612) was 148.2 kg.m^{-3}, with three internal thermocouples located at non-dimensional heights (L_i/L) of 0.25, 0.5, and 0.75. The post-test sample density was 144 kg.m^{-3}. Thermal conductivity data from the APA2-AS sample are compared to APA to evaluate effectiveness of aerogels in gas conduction heat transfer reduction.

The last sample considered here is Saffil.[TM,8] Saffil consists of high-purity un-needled polycrystalline alumina fibers in a matt, with a mean fiber diameter of 3 μm according to the manufacturer. It contains 95% to 97% alumina, and 3% to 5% silica by weight, with an overall density of 35 kg.m^{-3}. Saffil is provided in a roll with a width of 610 mm, and nominal matt thickness of 35 mm. Saffil can be easily compressed or pulled apart to obtain various sample thicknesses and densities for testing. Integrated thermal conductivity

---

[6] HeetShield, Inc.
[7] Morgan Thermal Ceramics
[8] Unifrax Ltd

data had been previously (Ref. 6) collected on three sample with thicknesses of 13.3 mm, 26.6 mm, and 13.3 mm, with corresponding densities of 24.2 kg.m^{-3}, 48 kg.m^{-3}, and 96.1 kg.m^{-3}, respectively. The mean fiber diameter was assumed to be 4.5 μm based on SEM data. The previous data are re-processed using the methodology used in this study.

7. Uncertainty Analysis

A detailed uncertainty analysis (Ref. 44) was conducted by taking into account the uncertainties of the measured quantities: hot- and cold-side temperatures, heat fluxes, and sample thickness. The overall uncertainty consisted of the contributions of precision and bias uncertainties for each measured quantity (T_H, T_C, q'', L) and uncertainties due to spatial nonuniformity of spatially-averaged quantities (T_H, T_C, q''). Using Eq. (18), the individual uncertainties for integrated thermal conductivity were calculated using

$$\Delta k_{int,j} = \left\{ \left(\frac{\partial k_{int}}{\partial L} \Delta L_j \right)^2 + \left(\frac{\partial k_{int}}{\partial q''} \Delta q''_j \right)^2 + \left(\frac{\partial k_{int}}{\partial T_H} \Delta T_{H\,j} \right)^2 + \left(\frac{\partial k_{int}}{\partial T_C} \Delta T_{C\,j} \right)^2 \right\}^{0.5} \tag{22.a}$$

where the subscript j stands for either bias (B), precision (P), or spatial nonuniformity (SN) uncertainty. The total uncertainty is then calculated using root sum square of the individual uncertainties (Ref. 44)

$$\Delta k_{int,U} = \left\{ \left(\Delta k_{int,B} \right)^2 + \left(\Delta k_{int,P} \right)^2 + \left(\Delta k_{int,SN} \right)^2 \right\}^{0.5} \tag{22.b}$$

The bias uncertainties used were 3.4% of reading for heat flux, 0.0254 mm for thickness, 1% of T_H reading for type C thermocouples, and 0.75% of T_C reading for type T thermocouples. The bias error for thermocouples was obtained from standard thermocouple tables, while the heat flux bias had been previously determined by calibration of select gauges against a high intensity solar constant lamp (Ref. 40). 120 temporal data points were typically used to calculate time-averaged quantities, and the precision error, P, for each measured quantity was determined by

$$P = t\,S \tag{22.c}$$

where S is the standard deviation associated with the time-averaged measured quantities, and t is obtained from t-distribution table for the appropriate number of degrees of freedom and 95% confidence interval. The spatial nonuniformity uncertainties were the standard deviations associated with the spatially-averaged measured quantities (T_H, T_C, q''). The precision and spatial nonuniformity uncertainties, and calculated total uncertainties determined for each set of data will be discussed for the various samples.

8. Results and Discussion

The experimental results and associated low-pressure thermal conductivity model for each of the test samples is provided. Thermal conductivity data as a function of pressure and temperature for the samples are generated using the standard model. Detailed thermal models for two samples are provided.

8.1. ZYF

The calculated integrated thermal conductivities and the corresponding measured temperatures (T_C, T_i) for the six septum-plate setpoint temperatures for LaRC Test 601 in vacuum (0.001 torr) are provided in Table 1 in the Appendix. The water-cooled plate temperatures, T_C, varied between 282.7 K and 286.6 K, with an average temperature of 284.3 K ±2.7 K for a 95% confidence interval. For each T_C, the corresponding temperatures at various non-dimensional heights (L_i/L) of 1, 0.727, 0.454, and 0.182 are provided in each row of the table. The calculated integrated thermal conductivity from Eq. (18) for each T_i is also provided in the table. The data from the table are shown in Figure 13, where the variation of k_{int} with T_i for various L_i/L locations is shown. Data for each L_i/L location is plotted using a different symbol. The error bars, used for the $L_i/L = 1$ data represent the experimental uncertainty. The precision uncertainties varied between 0.156% and 1.04% of reading for q'', 0.078% and 0.383% of reading for T_H, and between

17

0.006% and 0.015% for T_C. The spatial nonuniformity uncertainties varied between 3.05% and 7.61% of spatially averaged value of q'', 0.37% and 1.2% for T_H, and between 0.37% and 1.58% for T_C. The total uncertainty values calculated for k_{int} (T_H, T_c, 0.001 torr) for each septum plate setpoint temperature are listed in Table 1 ($\Delta k_{int, U}$). The total uncertainty (due to bias, precision, and spatial nonuniformity) varied between 9.1% at T_H of 535.8 K and 4.9% at T_H of 1640.1 K, with the uncertainty decreasing with increasing temperature. As seen in Figure 13, the k_{int} values for various L_i/L locations collapse to a single curve within the measurement uncertainty. If any of the data points fall far away from the curve, the data point should be discarded. A linear regression analysis was used in conjunction with Eq. (21) and the data in Table 1 to obtain the unknown coefficients for the low-pressure thermal conductivity of ZYF

$$k_{LP} = -5.415 \times 10^{-3} + 4.949 \times 10^{-5}T - 7.107 \times 10^{-8}T^2 + 6.037 \times 10^{-11}T^3 \qquad (23)$$

with k_{LP} in W.m^{-1}.K^{-1} and T in K. The low-pressure thermal conductivity of ZYF over the temperature range of 280 K and 1640 K for a sample density of 289 kg.m^{-3} is defined by Eq. (23). A plot of k_{LP} versus T is shown in Figure 14, where the non-linearity of k_{LP} with temperature is evident. The values of k_{LP} at various temperatures are presented in the first column of Table 2 in the Appendix. Since k_{LP} is calculated from k_{int}, it is assumed that the uncertainty in k_{LP} is equal to the maximum total uncertainty calculated for k_{int}, which is 9.1%.
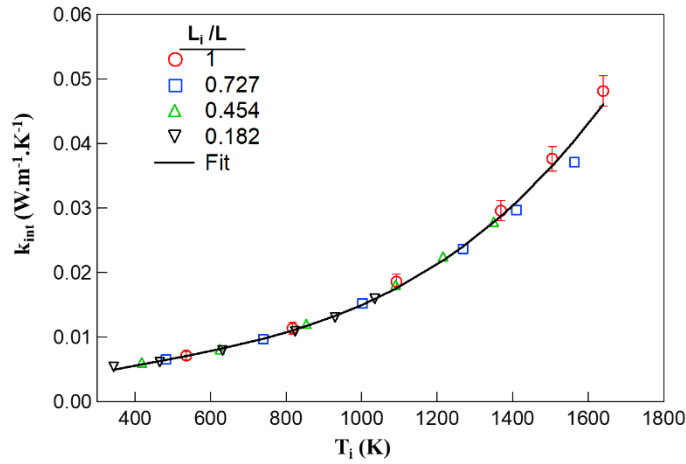

Figure 13. Variation of ZYF integrated thermal conductivity with internal sample temperatures in vacuum.
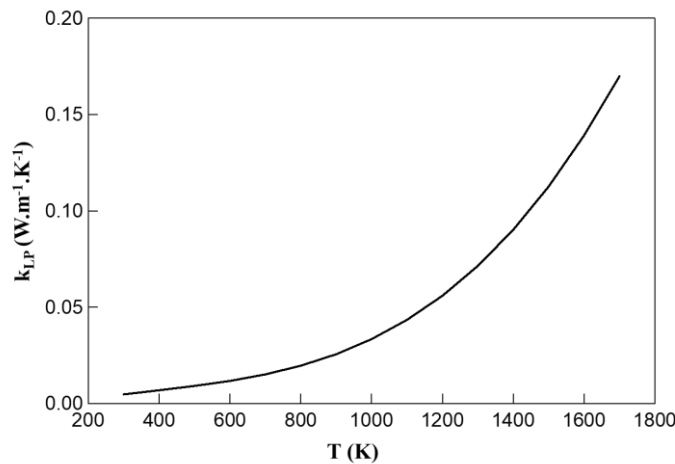
Figure 14. Variation of ZYF low-pressure thermal conductivity with temperature in vacuum.

A SEM of a ZYF sample with a magnification of 100 is shown in Figure 15. SEM images of 5 different areas of a ZYF sample with magnification factors of 1000 were used in conjunction with Image J[9] software to determine the fiber size distribution. The average fiber diameter using 90 different fibers from the images was determined to be 8.46 μm with a standard deviation of ±2.33 μm for a 95% confidence interval. The measured average fiber diameter is larger than the nominal range provided by the manufacturer (4 μm to 6 μm). Ideally, the diameter of the fiber should match the wavelength of peak radiation intensity according to Wein's displacement law (Ref. 31). For temperatures of 1000 K and 1900 K, the peak of radiation intensity occurs at 2.9 μm and 1.5 μm, respectively.

The fiber volume fraction for the ZYF sample was calculated from Eq. (6) to be 0.0515. This implies 94.8% void volume, verifying that ZYF is a high-porosity insulation. For the fiber volume fraction calculation, the sample density was 289 $kg.m^{-3}$, while the density of the bulk material was estimated using the rule of mixtures for the 89% zirconia and 10% yttria composition to be 5610 $kg.m^{-3}$. Using this fiber volume fraction and the calculated average fiber diameter, the pore size was calculated from Eq. (13) to be 1.29×10^{-1} mm. Typical fibrous insulation samples have pore sizes of the order of 0.1 mm.
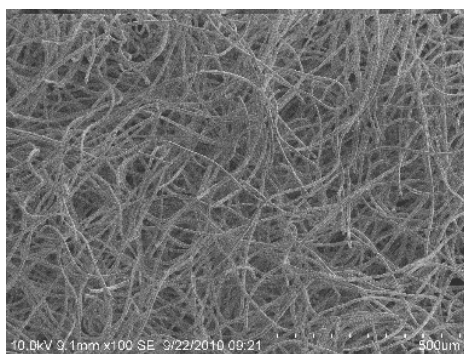

Figure 15. SEM of ZYF insulation.

The gas conduction thermal conductivity can be calculated from Eqs. (8-12) for any gas using the calculated pore size, and then added to the low-pressure thermal conductivity from Eq. (23) to obtain thermal conductivity as a function of temperature at various pressures. Table 2 contains values of thermal conductivity at various temperatures and pressures in dry air. A plot of thermal conductivity of ZYF as a function of temperature for various pressures in dry air is presented in Figure 16. As pressure increases the thermal conductivity curves shift to higher values in the figure. Most of the shifts are by small increments, but a significant change in thermal conductivity data is observed between 0.76 and 38 torr. A plot showing variation of thermal conductivity of ZYF with pressure at a constant temperature of 1200 K in dry air is shown in Figure 17. Thermal conductivity of ZYF at 0.001 torr is 0.056 $W.m^{-1}.K^{-1}$, stays relatively constant up to 0.1 torr, after which it rises rapidly to 0.127 $W.m^{-1}.K^{-1}$ at 76 torr, then gradually increases to 0.131 $W.m^{-1}.K^{-1}$ at 760 torr. This behavior is typical of fibrous insulation samples with pore size of the order of 0.1 mm. As discussed before, three distinct regions are present: rarefied gas conduction regime between 10^{-3} torr and 0.1 torr where thermal conductivity does not vary appreciably with pressure, gas conduction transition region between 0.1 torr and 100 torr where thermal conductivity varies significantly with pressure, and finally the continuum region above 100 torr where thermal conductivity does not vary significantly with pressure.

A plot of ZYF thermal conductivity versus temperature at 7.6 torr pressure in six different gases (dry air, nitrogen, argon, carbon dioxide, hydrogen, and helium) is shown in Figure 18. The thermal conductivity of the insulation is lowest in argon, and highest in hydrogen. The thermal conductivities in air and nitrogen are similar, with thermal conductivity in carbon dioxide slightly higher than the thermal conductivity in air.

---

[9] Public domain software from the National Institute of Health
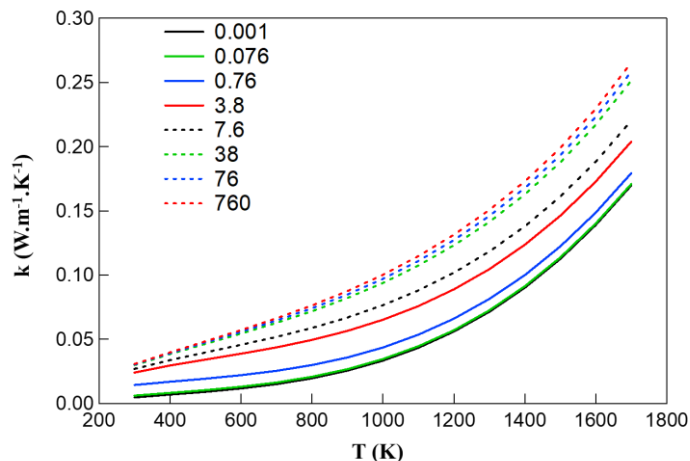
Figure 16. Variation of ZYF thermal conductivity with temperature and static pressure in dry air.
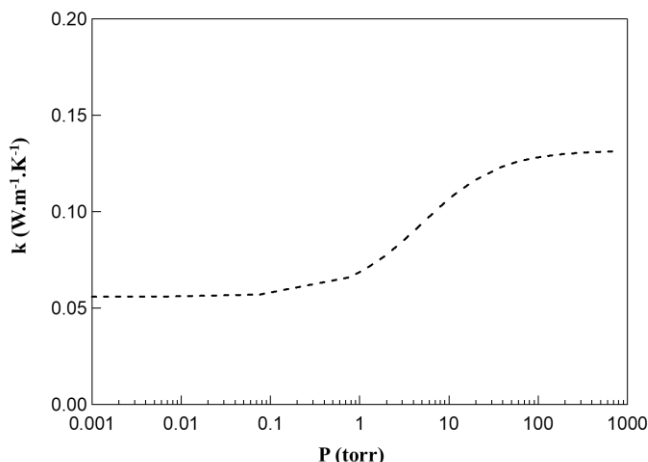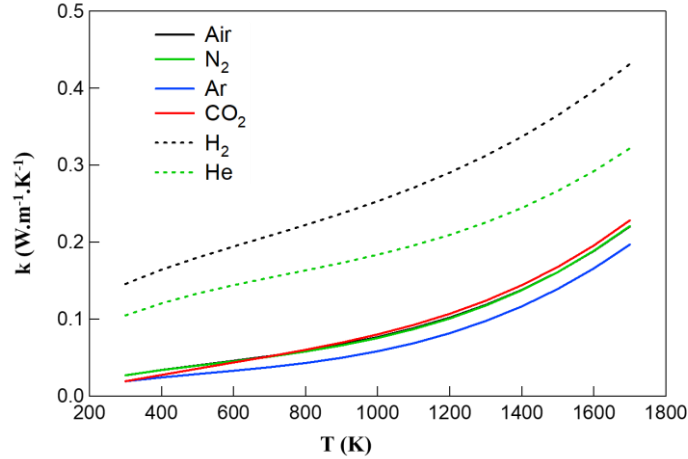

Figure 17. Variation of ZYF thermal conductivity with static pressure at 1200 K in dry air.

The thermal conductivity in helium is second highest. Most commercial laboratories provide thermal conductivity data in either argon or nitrogen gas. Based on the observed differences between the thermal conductivity of fibrous insulation in various gases, the thermal conductivity data from commercial laboratories should be generated in the intended use gaseous medium. For example, if the insulation is supposed to be used in a helium environment, one cannot rely on thermal conductivity data generated in argon. Better approach will be to follow the approach proposed here: measure thermal conductivity in vacuum, estimate pore size, then calculate gas conduction contributions at various pressures in various gases using the formulation provided here.

The calculated low-pressure thermal conductivity of ZYF from LaRC Test 601 is compared with previous results from LaRC Test 540 (Ref. 6) in Figure 19. The results are similar, with LaRC Test 540 having slightly higher thermal conductivity than Test 601. Test 540 results are outside the ±9.1% uncertainty range over the temperature range of 900 K to 1200 K. However, the measured densities of the two samples were different: 289 kg.m^{-3} and 270.8 kg.m^{-3} for LaRC Tests 601 and 540, respectively. The thermal conductivity comparison of samples with different densities is not a fair or valid comparison, since a sample with higher density will typically have a lower thermal conductivity. Heat transfer in high-porosity insulations at high temperatures in vacuum is dominated by radiation, and the radiant thermal conductivity is inversely

Figure 18. Variation of ZYF thermal conductivity with temperature in different gases at a static pressure of 7.6 torr.

proportional to sample density. It cannot be determined if the lower thermal conductivity of a sample is due to better thermal performance or due to added mass. Comparing the product of density and thermal conductivity ($\rho.k$) is a valid comparison. For steady-state heat transfer, the product of thermal conductivity and density has been shown to be proportional to the mass of insulation required per unit area (Ref. 45). The comparison of $\rho.k$ for the two samples is provided in Figure 20. LaRC Test 540 results are slightly higher than Test 601 results, but within the uncertainty range over the entire temperature range. The close agreement between the two test samples in Figure 20 implies that the testing and analysis is repeatable, especially since the test setup has gone through some major modifications between the two tests.

For detailed modeling, separating the low-pressure thermal conductivity into its solid conduction and radiation components, Eqs. (5, 7, and 14) are utilized to estimate F and e/n^{*2}. Cryogenic and high-temperature thermal conductivity data (both in vacuum) should be used for estimation of F and e/n^{*2}. The cryogenic thermal conductivity data in vacuum are solid conduction dominated, while data above 1000 K in vacuum are radiation dominated. The cryogenic thermal diffusivity of a ZYF sample in vacuum had been measured over the temperature range of 90 K to 230 K using the three-point step heating technique (Ref. 23) by a commercial laboratory (Ref. 46). The reported sample density was 251 kg.m^{-3}, which is lower than
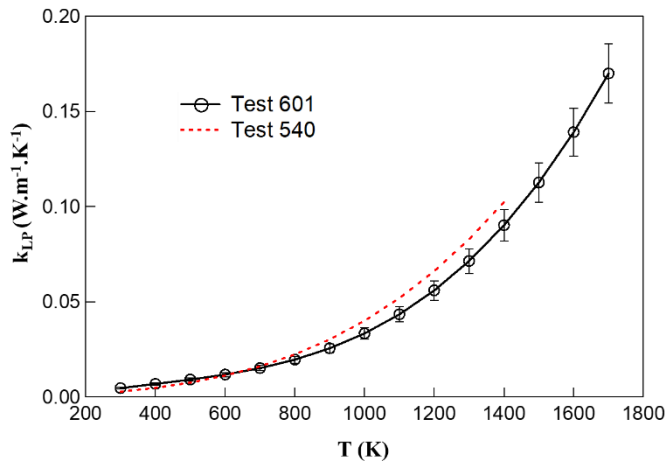
Figure 19. Comparison of variation of ZYF k_{LP} with temperature for two tests in vacuum (densities of 289 kg.m^{-3} and 270.8 kg.m^{-3} for Tests 601 and 540, respectively).

21
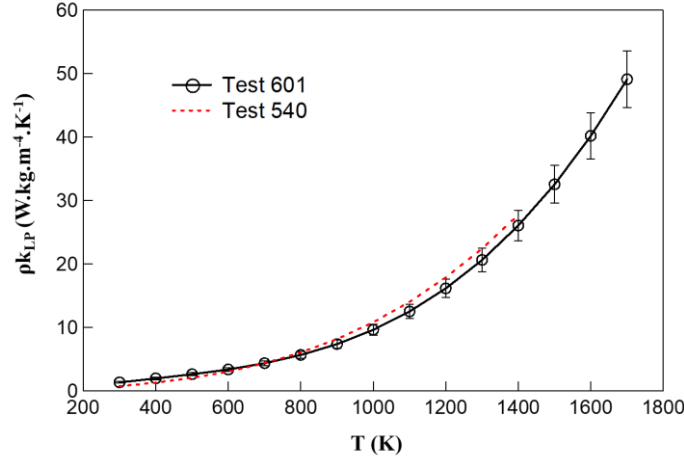
Figure 20. Comparison of variation of ZYF $\rho.k_{LP}$ with temperature for two tests in vacuum (densities of 289 kg.m^{-3} and 270.8 kg.m^{-3} for Tests 601 and 540, respectively).

the densities for the two LaRC test samples (289 kg.m^{-3} and 270.8 kg.m^{-3}), but closer to the manufacturer specified nominal value of 240 kg.m^{-3}. The sample specific heat had also been measured using the differential scanning calorimetry technique (Ref. 24) by the same laboratory. The cryogenic specific heat of zirconia-yttria compound was also calculated using the rule of mixtures applied to the specific heat data of zirconia (89%) and yttria (10%) from Ref. 47 over the temperature range of 80 K to 300 K, which was best fit with a second order polynomial using regression analysis

$$c_P = -93.976 + 2.911\,T - 3.629 \times 10^{-3}T^2 \tag{24}$$

where c_p is in J.kg^{-1}.K^{-1} and T in K. A comparison of measured specific heat data from Ref. 46 with predictions of specific heat from Eq. (24) is shown in Figure 21. Close agreement between the data sets is observed, with a root mean square deviation (RMSD) of 2.9%. The error bars in the figure correspond to reported measurement uncertainty of ±4% from Ref. 46. The measured thermal diffusivity, specific heat, and density from Ref. 46 were used to calculate the low-pressure thermal conductivity of ZYF from 90 K to 230 K, with the results presented in Table 3 in the Appendix. The bulk thermal conductivity of ZYF (yttria-stabilized zirconia) is needed in Eq. (5). No source of data was found for thermal conductivity of this specific compound (89% zirconia and 10% yttria) over the desired temperature range of 100 K to 1700K. A combination of data from various sources was used to generate this property over the desired temperature range. Curve 5 of Touloukian's data for pure zirconia (Ref. 33, pp. 246-249) was used for the temperature range of 1513 K to 2103 K. Curve 1 of Touloukian's data for 85% zirconia and 15% yttria (Ref. 33, pp. 499-451) was used for the temperature range of 477 K to 1366 K. Popov et al, (Ref. 48) have measured thermal conductivity of single crystal zirconia-yttria for yttria concentrations of 0.5% to 8% from 50 K to 300 K, showing that the thermal conductivity decreases with increasing yttria concentration. Popov's 8% yttria concentration data is closest to the 10% yttria concentration in ZYF, but the slope of the thermal conductivity data versus temperature for Popov's data was too high to match the remaining selected data from 477 K to 2103 K. Only the 100 K data point from Popov's data for the 8% yttria concentration was used. The resulting combination of data points from the three sources is shown graphically in Figure 22. The best linear fit of data was obtained using regression analysis for the bulk thermal conductivity of zirconia-yttria compound for the temperature range of 100 K to 2100 K
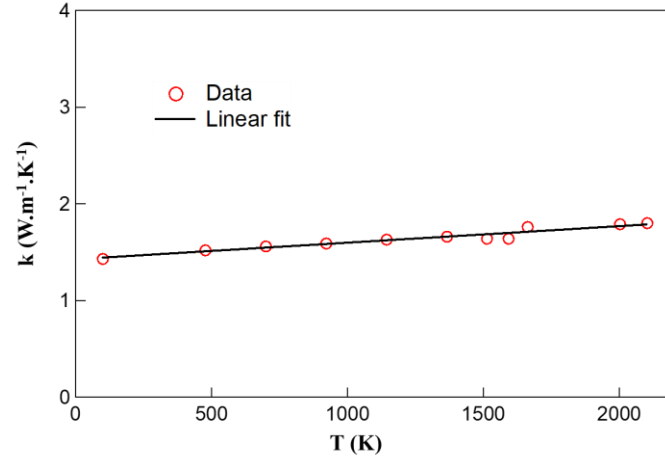
$$k_b = 1.428 + 1.712 \times 10^{-4}T \tag{25}$$

with k_b in W.m^{-1}.K^{-1} and T in K. The best linear fit is also shown in Figure 22. Combining Eqs. (5, 7, and 14) yields

$$k_{LP} = Ffk_b(T) + \frac{16\,\sigma\,T^3}{3\rho_T(\frac{e}{n^{*2}})}$$ (26)
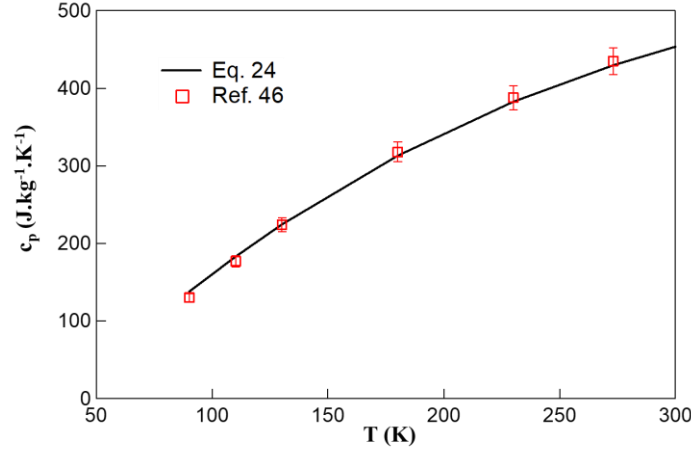
Figure 21. Variation of ZYF specific heat with temperature.

Figure 22. Variation of ZYF bulk material thermal conductivity with temperature.

The fiber material goes through linear expansion and contraction over the wide temperature range of 100 K to 2000 K, but it is assumed that the sample density for this high-porosity insulation stays constant with temperature. F is assumed to be constant, and that the quantity e/n^{*2} is assumed to be a third order polynomial function of temperature

$$\frac{e}{n^{*2}} = \Sigma_{i=0}^{3} c_i T^i$$ (27)

There are five unknown parameters in Eq. (26). The genetic algorithm optimization procedure (Refs. 49, 50) was used to estimate the five unknown parameters, F_s, and $c_i\,(i=[0,3])$ in conjunction with cryogenic thermal conductivity data from Table 3 at a density of 251 kg.m^{-3}, and the 0.001 torr thermal conductivity data from Table 2 at a density of 289 kg.m^{-3}. The best fit of data for F and e/n^{*2} are

$$F = 4.793 \times 10^{-2}$$ (28.a)

$$\frac{e}{n^{*2}} = 9.859 + 5.917 \times 10^{-2}T - 4.280 \times 10^{-5}T^2 + 8.956 \times 10^{-9}T^3$$ (28.b)

with F being non-dimensional, e/n^{*2} in $m^2.kg^{-1}$, and T in K. The variation of e/n^{*2} with temperature is shown graphically in Figure 23. The quantity e/n^{*2} increases with temperature up to 1000 K, then decreases with increasing temperature above 1000 K. The comparison of calculated k_{LP} from Eq. (26) with standard model data from Tables 2 and 3 (data used for the parameter estimation) is provided in Figure 24. The error bars in the figure correspond to the $\pm9.1\%$ uncertainty associated with standard model for ZYF. The comparison over the temperature range of 100 K to 1700 K is shown in Figure 24.a, which reveals a satisfactory fit of data with a RMSD of 12.6% over the entire temperature range. The differences varied between 7.5% at 600 K and 0.8% at 1700K, with the differences decreasing with increasing temperature. The RMSD between detailed and standard models was 4.6% for temperatures between 300 K and 1700 K, indicating that the procedure used for obtaining solid conduction and radiation parameters yields satisfactory results above 300 K. The comparison of data over the temperature range of 100 K to 500 K is shown in Figure 24.b which better reveals differences between the data and detailed model at lower temperatures with a resulting RMSD of 19.7% over this temperature range. The uncertainties in solid conduction model are higher at lower temperatures due to uncertainties in cryogenic thermal diffusivity measurements and thermal conductivity of bulk material at cryogenic temperatures. The observed discontinuity in the curve at 300 K in Figure 24.b is due to the use of two distinct density values above and below 300 K (289 kg.m^{-3} and 251 kg.m^{-3}).
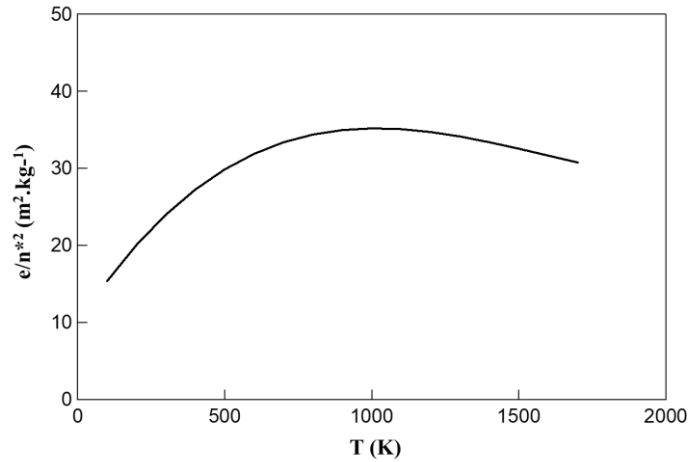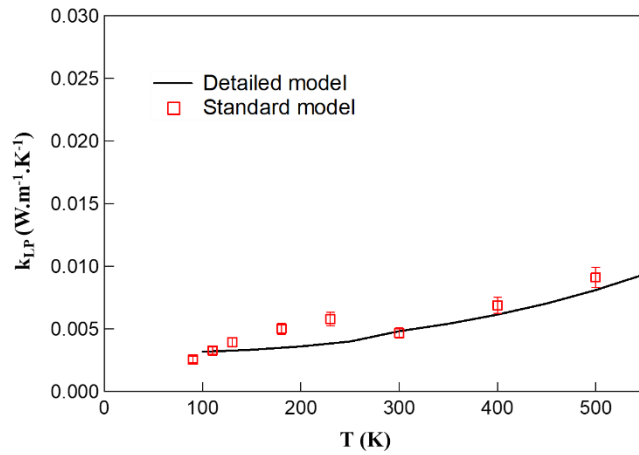

Figure 23. Variation of ZYF e/n^{*2} with temperature.

The ratios of solid conduction and radiation thermal conductivity to k_{LP} (k_s/k_{LP} and k_r/k_{LP}) at 0.001 torr for ZYF insulation density of 289 kg.m^{-3} are shown in Figure 25. Solid conduction is a significant mode of heat transfer in ZYF in vacuum, with 98% of heat transfer due to solid conduction at 100 K, with solid conduction's significance decreasing with increasing temperature. Solid conduction contribution drops below 10% of heat transfer above 1100 K and equals 2.5% of heat transfer at 1700 K. Radiation starts at 2% at 100K, and increases with increasing temperature, reaching 97.5% at 1700 K. Radiation and solid conduction contributions are equal at 470 K.

Thermal conductivity of ZYF at 289 kg.m^{-3} at various temperatures, pressures, and in various gases can be generated using the low-pressure thermal conductivity from Eq. (23) and pore size of 1.29×10^{-4} m. The low-pressure thermal conductivity can be further broken down into its radiation and solid conduction components according to Eq. (26), with the unknown parameters estimated using genetic algorithm optimization in conjunction with cryogenic and high-temperature ($T \geq 300$ K) thermal conductivity data in vacuum. The unknown parameter estimates for this insulation are provided in Eqs. (28.a and 28.b). The major sources of uncertainty for the latter approach are the cryogenic thermal diffusivity data and the thermal conductivity of bulk material at cryogenic temperatures.
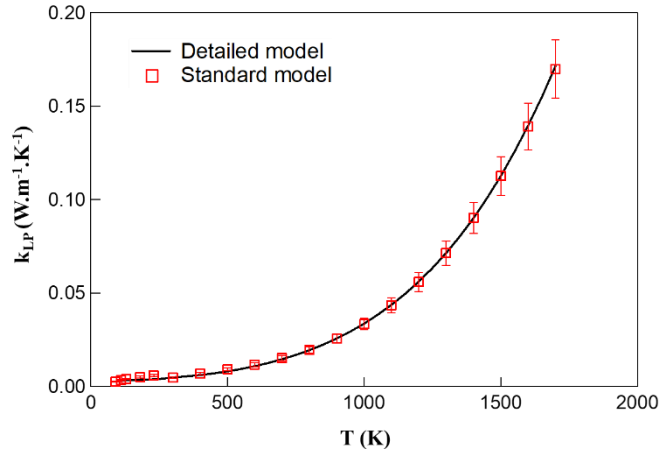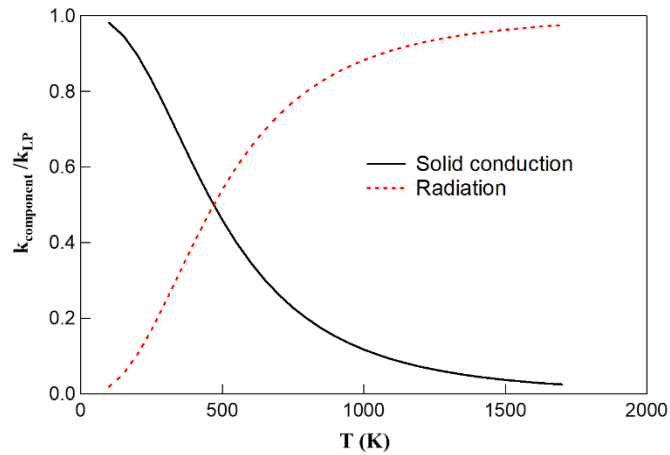
a)

b)

Figure 24. Comparison of ZYF detailed and standard models in vacuum for temperature ranges of: a) 100 K to 1700 K, b) 100 K to 500 K.

Figure 25. Variation of ratio of solid conduction and radiation thermal conductivity to k_{LP} with temperature in vacuum for ZYF.

25

8.2 APA

The calculated integrated thermal conductivities for LaRC Test 602 in vacuum (0.001 torr), and the resulting low-pressure thermal conductivities did not follow the expected patterns. The erroneous data could have been caused by some of the data acquired when test conditions had not reached steady-state conditions. So, a more complicated procedure had to be used to estimate k_{LP}. The integrated thermal conductivity data at 0.1 torr were utilized, and then corrected by subtracting the contributions of gas conduction in nitrogen gas at this higher pressure to calculate the low-pressure thermal conductivity. The variation of calculated integrated thermal conductivity data with measured internal temperatures at 0.1 torr pressure is shown in Figure 26. Integrated thermal conductivity data were obtained at non-dimensional heights of 1, 0.714, 0.476, and 0.238. The corresponding T_C for these measurements varied between 283.1 K and 291.4 K, with an average value of 287.6 K ±6.4 K for a 95% confidence interval. The error bars used for the $L_i/L = 1$ data in the figure represent the total experimental uncertainty. The precision uncertainties varied between 0.383% and 2.46% of reading for q'', 0.015% and 0.025% for T_H, and between 0.026% and 0.027% for T_C. The spatial nonuniformity uncertainties varied between 3.25% and 4.49% of spatially averaged value of q'', 0.58% and 1.57% for T_H, and between 0.14% and 0.79% for T_C. The total uncertainty values calculated for k_{int} (T_H, T_c, 0.1 torr) for each septum plate setpoint temperature varied between 7.1% at T_H of 813.3 K and 11.7% at T_H of 1648.5 K, with the uncertainty increasing with increasing temperature. The k_{int} values at various depths collapsed to a single curve within the measurement uncertainty as seen in Figure 26. A regression analysis was used in conjunction with Eq. (21) and data in Figure 26 to obtain the unknown coefficients for the thermal conductivity of APA at 0.1 torr, resulting in

$$k(T, 0.1\ torr) = -1.03 \times 10^{-2} + 7.372 \times 10^{-5}T - 1.028 \times 10^{-7}T^2 + 9.852 \times 10^{-11}T^3 \quad (29)$$

with k in W.m^{-1}.K^{-1} and T in K. The mean fiber diameter of APA has been determined to be 3.2 μm from SEM images of APA (Ref. 15). APA's 3.2 μm mean fiber diameter is better suited for high-temperature application because it matches the wavelength of peak radiation intensity at 900 K. The fiber volume fraction for the APA sample was calculated from Eq. (6) to be 0.0308. For the fiber volume fraction calculation, the sample density was 98.4 kg.m^{-3} while the density of the bulk material was estimated using the rule of mixtures to be 3200 kg.m^{-3} for the specific composition of APA (86% alumina and 10% silica). Using the calculated fiber volume fraction and average fiber diameter, the pore size was calculated from Eq. (13) to be 8.16×10^{-5} m, which is in the typical range for fibrous insulation samples. Using the determined pore size, the gas conduction thermal conductivity at 0.1 torr in nitrogen gas (gaseous medium for the tests) was calculated from Eqs. (8-12), and then subtracted from the thermal conductivity data provided in Eq. (29), to obtain the low-pressure thermal conductivity

$$k_{LP} = -1.180 \times 10^{-2} + 7.466 \times 10^{-5}T - 1.034 \times 10^{-7}T^2 + 9.867 \times 10^{-11}T^3 \quad (30)$$

with k_{LP} in W.m^{-1}.K^{-1} and T in K. It is assumed that the total uncertainty of k_{LP} and thermal conductivity at higher pressures for APA equal the maximum total uncertainty calculated for k_{int}, which is 11.7%.

To validate the calculated pore size of 8.16×10^{-5} m from Eq. (13) for APA, the following procedure was used. Test data were generated at various pressures for T_H setpoint temperatures of 800 K, 1360 K, and 1640 K. At each setpoint temperature, data were generated at the following nominal pressures: 0.001 torr, 0.1 torr, 1 torr, 5 torr, 10 torr, 50 torr, 100 torr, and 300 torr. A plot showing variation of k_{int} versus pressure obtained at non-dimensional heights (L_i/L) of 1, 0.714, 0.476, and 0.238 for the setpoint temperature of 1640 K is shown in Figure 27. Using κ of 8.16×10^{-5} m, k_g was calculated from Eq. (8), added to k_{LP} from Eq. (30), then integrated using Eq. (19) for each of the corresponding sets of input data (T_i, T_c, P) to estimate k_{int} and then compare with measured k_{int} from experimental data. The trapezoidal rule was used for the numerical integration of Eq. (19), and the entire data set for the three hot-side temperature setpoints were used. The difference between estimated and measured k_{int} varied between -7.4% and 3.3%, with a RMSD of 3.1%. The close agreement validates the use of Eq. (13) for calculating the pore size.
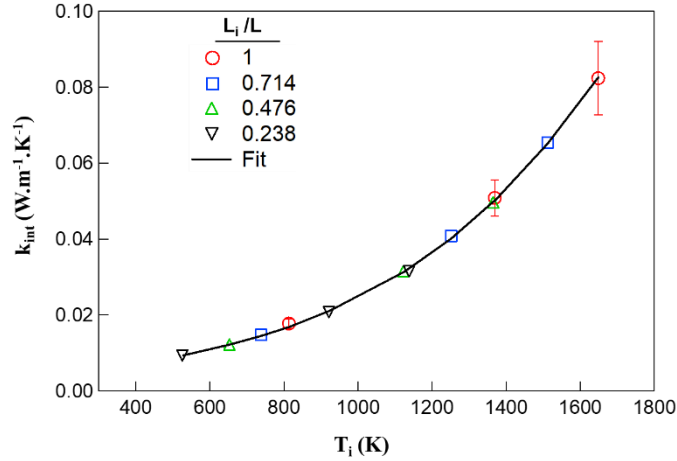
Figure 26. Variation of APA integrated thermal conductivity with internal sample temperatures at 0.1 torr static pressure in nitrogen.
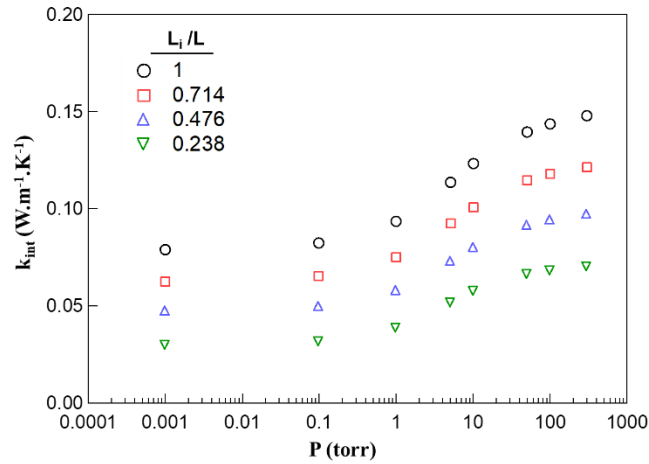

Figure 27. Variation of APA integrated thermal conductivity with static pressure in nitrogen for $T_H = 1640$ K.

Using k_{LP} from Eq. (30) and κ of 8.16×10^{-5} m, thermal conductivity data were calculated as a function of temperature for various pressures in dry air and presented in Table 4 in the Appendix and Figure 28. The low-pressure thermal conductivity is nonlinear, increasing rapidly at higher temperatures due to the contribution of the radiation component of heat transfer. As pressure increases, the curves for various pressures shift to higher values. A plot showing variation of thermal conductivity with pressure at a constant temperature of 1400 K in dry air is shown in Figure 29 which shows similar trends as previously observed with ZYF insulation in Figure 17. Thermal conductivity of APA at 0.001 torr is 0.161 W.m^{-1}.K^{-1}, stays relatively constant up to 0.1 torr, after which it rises rapidly to 0.199 W.m^{-1}.K^{-1} at 76 torr, then gradually increases to 0.243 W.m^{-1}.K^{-1} at 760 torr. At the lowest pressure values, $P < 0.1$ torr, the thermal conductivity is due to solid conduction and radiation modes of heat transfer. As pressure increases beyond 0.1 torr, gas conduction contribution begins, but it does not reach the complete gas conduction contribution level until $P > 100$ torr. This behavior is typical of fibrous insulation samples with pore size of the order of 0.1 mm.
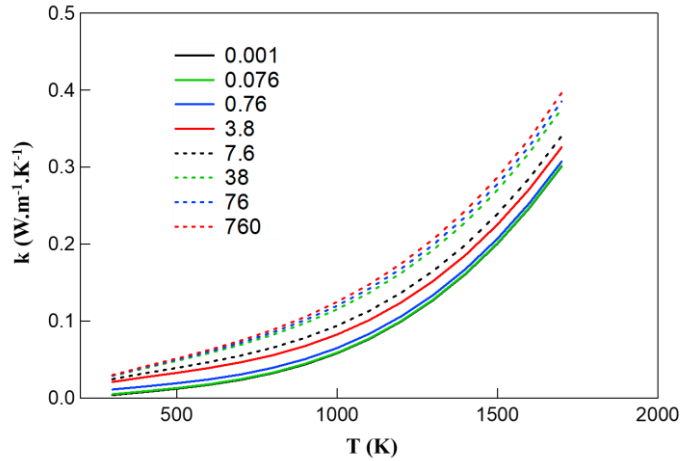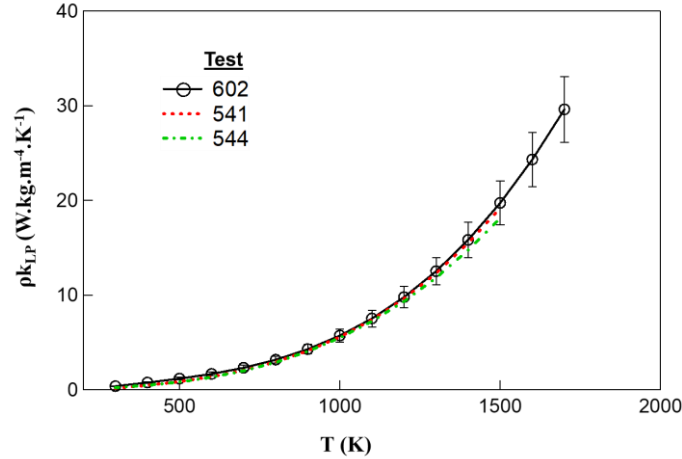
Figure 28. Variation of APA thermal conductivity with temperature and static pressure in dry air.
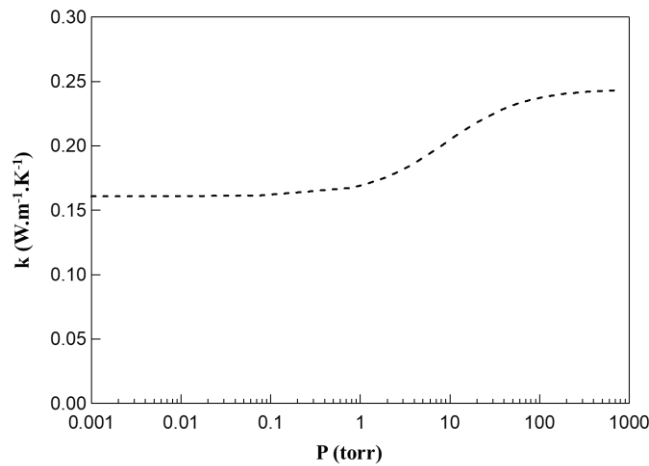
Figure 29. Variation of APA thermal conductivity with static pressure at 1400 K in dry air.

Data from LaRC Test 602 were then compared with previous low-pressure thermal conductivity data from LaRC Tests 541 and 544. LaRC Test 541 sample had a density of 107 kg.m^{-3} with no internal thermocouples, while LaRC Test 544 sample had a density of 108 kg.m^{-3} with 4 internal thermocouples, while LaRC Test 602 had a density of 98.4 kg.m^{-3} with three internal thermocouples. To account for the variation of density between the three samples, the comparison of the product of density and low-pressure thermal conductivity for the three tests is provided in Figure 30. Data for the three tests agree within the 11.7% experimental uncertainty. The LaRC Test 541 $\rho.k_{LP}$ data differ from LaRC Test 602 data between 17.7% at 600 K and 2.7% at 1400 K, with a RMSD of 7.7%. The LaRC Test 544 $\rho.k_{LP}$ data differ from LaRC Test 602 data between 21% at 600 K and 8.2% at 1400 K, with a RMSD of 10.1%. The observed close agreement between tests proves that the tests are repeatable as long as variations in density are accounted for, and that results are similar irrespective of number of internal thermocouples used; four, three, or none. But use of at least three to four internal thermocouples provides additional integrated thermal conductivity data at each test setpoint temperature, and additional data can result in higher confidence in the inferred thermal conductivity data.

Figure 30. Comparison of variation of APA $\rho.k_{LP}$ with temperature for three tests in vacuum (densities of 98.4 kg.m^{-3}, 107 kg.m-3, and 108 kg.m^{-3} for Tests 602, 541, and 540, respectively).

The comparison of the product of density and low-pressure thermal conductivity for ZYF and APA is provided in Figure 31. APA has lower $\rho.k_{LP}$ compared to ZYF, with the difference increasing with increasing temperature. The $\rho.k_{LP}$ of APA is 69% to 66% lower than ZYF in the 1000 K to 1700 K range. This observation implies that the radiation contribution to overall heat transfer is lower in APA compared to ZYF. The lower radiation heat transfer could be due to better optical properties for APA and the smaller mean fiber diameter of APA, 3.2 µm for APA compared to 8.46 µm for ZFY. The lower diameter of APA is within the range of dominant radiation wavelengths at high-temperatures and could result in higher attenuation of radiation heat transfer.
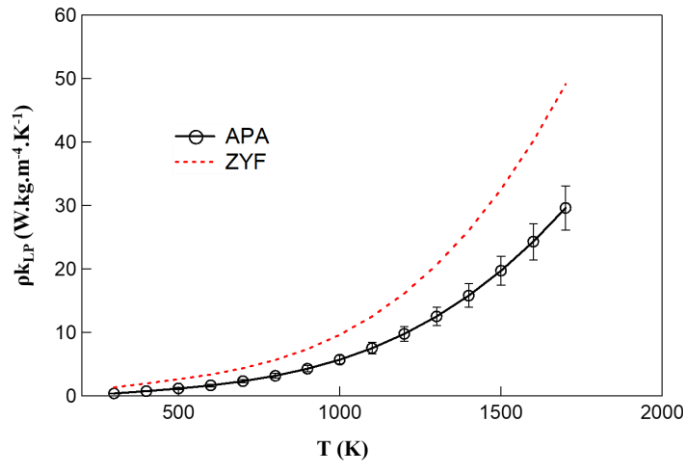
Figure 31. Comparison of variation of APA and ZYF $\rho.k_{LP}$ with temperature.

Cryogenic thermal conductivity data of APA and thermal conductivity of the bulk material are needed to construct the solid conduction and radiation models of APA for the detailed model. The cryogenic thermal diffusivity of an APA-1 sample in vacuum had been measured over the temperature range of 130 K to 270 K using the three-point step heating technique (Ref. 23) by a commercial laboratory (Ref. 51). The reported sample density was 112 kg.m^{-3}, which is slightly higher than the densities for the two LaRC samples for Tests 541 and 544 (107 kg.m^{-3} and 108 kg.m^{-3}). The sample specific heat had also been measured using the differential scanning calorimetry technique (Ref. 24) by the same laboratory. The specific heat of APA was also calculated using the rule of mixtures applied to the specific heat data of

alumina (86%) and silica (10%) from Ref. 47 over the temperature range of 100 K to 1500 K, which was best fit with a fourth order polynomial

$$c_P = -371.1 + 5.841T - 8.4 \times 10^{-3}T^2 + 5.418 \times 10^{-6}T^3 - 1.285 \times 10^{-9}T^4 \qquad (31)$$

where c_p is in J.kg^{-1}.K^{-1} and T in K. Comparison of measured specific heat data from Ref. 51 with predictions of specific heat from Eq. (31) is shown in Figure 32, with the error bars corresponding to the reported ±4% measurement uncertainty (Ref. 51). There is close agreement between the data sets, with a RMSD of 2.7%. The measured thermal diffusivity, specific heat, and density from Ref. 51 were used to calculate the low-pressure thermal conductivity of APA from 130 K to 273 K, with the results presented in Table 5 in the Appendix.

The bulk thermal conductivity of alumina/silica (86% alumina, 10% silica) compound is also needed. No source of data was found for thermal conductivity of this specific compound. Unlike specific heat calculations for compounds, the rule of mixtures cannot be used to estimate thermal conductivity of compounds from the constituents' properties. It should be noted that at cryogenic temperatures the thermal conductivity of alumina varies with impurity content (Refs. 52, 53), as was the case with zirconia. Due to lack of data for this specific compound, the recommended thermal conductivity data for pure alumina from Ref. 33 was used for the temperature range of 100 K to 2000 K. The variation of the alumina thermal conductivity with temperature from Ref. 33 is shown in Figure 33, and was fit using regression analysis

$$k_b = -4.39873 + \frac{12832.79}{T} \qquad (32)$$

where T is in K and k_b in W.m^{-1}.K^{-1}.
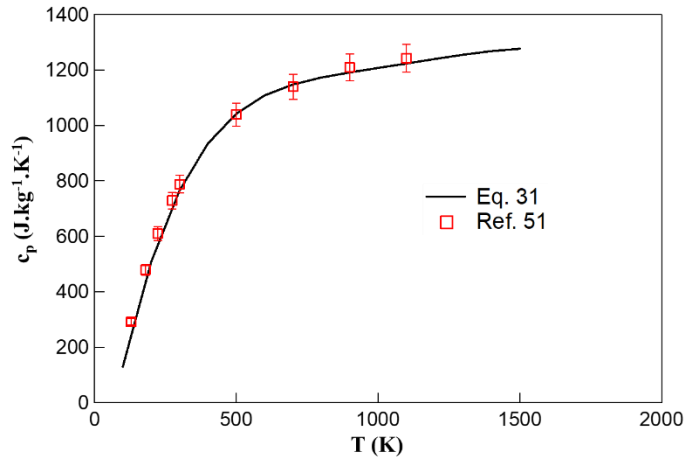
**Figure 32. Variation of APA specific heat with temperature.**

30
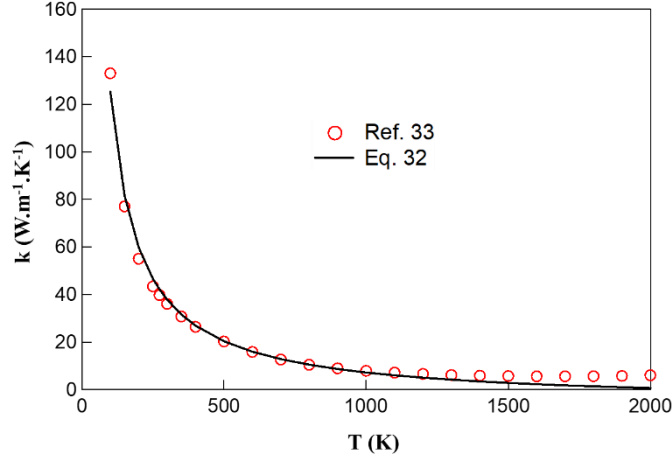
Figure 33. Variation of APA bulk material thermal conductivity with temperature.

Assuming the quantity e/n^{*2} for APA is also a third order polynomial function of temperature, as in Eq. (27), there are five unknown parameters in Eq. (26): F, and c_i ($i= [0,3]$). Similar to the ZYF detailed modeling analysis, the genetic algorithm optimization procedure was used to estimate the 5 unknown parameters in conjunction with cryogenic thermal conductivity data from Table 5 at a density of 112 kg.m^{-3}, and the 0.001 torr thermal conductivity data from Table 4 at a density of 98.6 kg.m^{-3}. The best fit for F and e/n^{*2} are

$$F = 5.676 \times 10^{-4} \tag{33.a}$$

$$\frac{e}{n^{*2}} = 8.738 + 7.782 \times 10^{-2}T - 4.248 \times 10^{-5}T^2 + 6.536 \times 10^{-9}T^3 \tag{33.b}$$

with F being non-dimensional, e/n^{*2} in m^2.kg^{-1}, and T in K. The variation of e/n^{*2} with temperature is shown graphically in Figure 34. e/n^{*2} for APA starts at 16.1 m^2.kg^{-1} at 100 K, reaches a maximum of 52.5 m^2.kg^{-1} at 1300 K, then decreases to 50.4 m^2.kg^{-1} at 1700 K. The quantity e/n^{*2} for ZYF is also shown in Figure 34 for comparison. As expected, APA has higher e/n^{*2} values compared to ZYF at all temperatures, indicating that it is more efficient in attenuating radiation heat transfer due to its smaller mean diameter size and better optical properties. Note that the radiation thermal conductivity is inversely proportional to e/n^{*2} from Eq. (7). The higher the value of e/n^{*2}, the lower the radiant thermal conductivity.
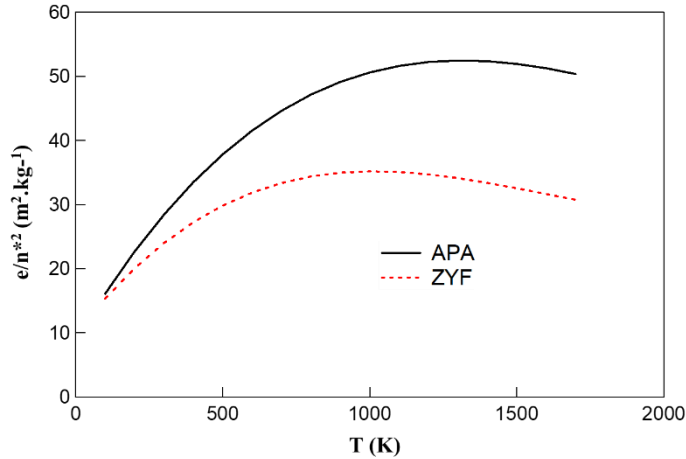

Figure 34. Comparison of variation of APA and ZYF e/n^{*2} with temperature.

31

The comparison of predicted low-pressure thermal conductivity from the detailed model versus the standard model data from Tables 4 and 5 over the temperature range of 100 K to 1700 K is shown in Figure 35. The error bars in the figure correspond to the ±11.7% uncertainty associated with the standard model for APA. The RMSD deviation between detailed model and data was 31.6% over the entire temperature range, as seen in Figure 35.a. The deviations varied between 4.9% and 0.4% between 600 K and 1700 K, with the deviations generally decreasing with increasing temperature. The RMSD between detailed and standard models was 7.1% for temperatures between 300 K and 1700 K, indicating that the procedure used for obtaining solid conduction and radiation parameters yields satisfactory results above 300 K. The comparison over the low-temperature region of 130 K to 500 K is shown in Figure 35.b, showing the differences between the detailed and standard models at lower temperatures. The RMSD between data and detailed model for 130 K $< T <$ 500 K was 52.1%. The uncertainties in solid conduction model are higher at lower temperatures due to uncertainties in cryogenic thermal diffusivity measurements and thermal conductivity of bulk material at cryogenic temperatures. The observed discontinuity at 300 K in the figure is due to the difference in sample densities below and above this point: 112 kg.m^{-3} below 300 K and 98.4 kg.m^{-3} above 300 K.
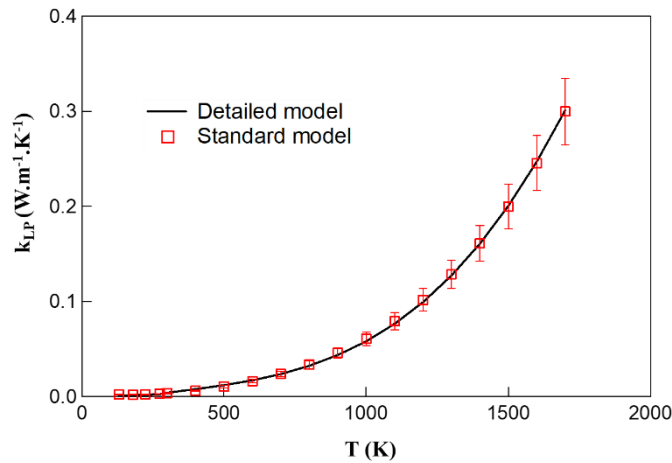

a)
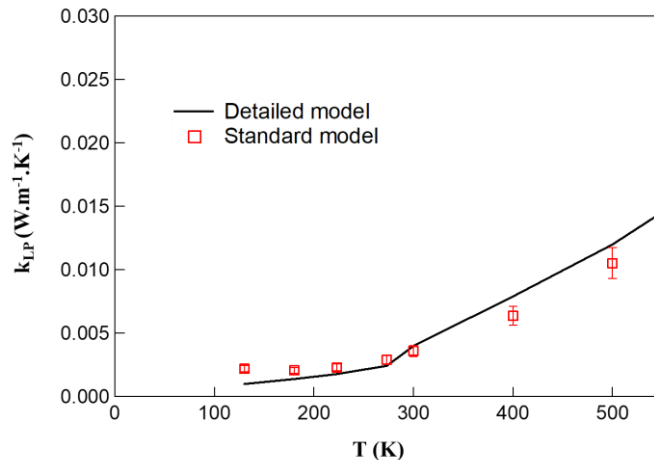
b)

Figure 35. Comparison of APA detailed and standard models in vacuum for temperature ranges of: a) 100 K to 1700 K, b) 100 K to 500 K.

The ratios of solid conduction and radiation thermal conductivity to k_{LP} (k_s/k_{LP} and k_r/k_{LP}) at 0.001 torr for APA with insulation density of 98.4 kg.m^{-3} are shown in Figure 36. Solid conduction constitutes 92% of heat transfer at 100 K and decreases with increasing temperature. Solid conduction falls below 50% above 200 K, equals 18.7% at 300 K, and falls below 1% above 800 K. Radiation is the dominant mode of heat transfer in this insulation above 300 K, increasing from 81.3% at 300 K to 99% at 800 K. The crossover point is at 197 K.

The thermal conductivity of an APA sample at a density of 112 kg.m^{-3} had been measured at a pressure of 5×10^{-3} torr for temperatures between 300 K and 1100 K using the three-point step heating technique (Ref. 23) by a commercial laboratory (Ref. 54). The detailed model for APA was used with a density of 112 kg.m^{-3} and pressure of 5×10^{-3} torr to predict thermal conductivity as a function of temperature. The comparison of predicted and measured thermal conductivities for this sample are provided in Figure 37. The error bars correspond to the reported ±12% uncertainty for the experimental data (Ref. 54). The difference between predicted and measured values varied between 12.4% at 300 K and 0.6% at 1100 K, with a RMSD of 6.4%. The close agreement between predictions and measurements by an independent laboratory, validate the thermal testing and modeling approach used in this report.
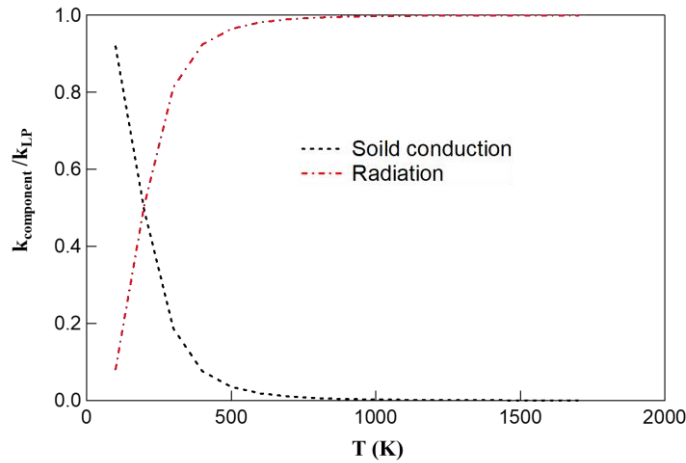
Figure 36. Variation of ratio of solid conduction and radiation thermal conductivity to k_{LP} with temperature in vacuum for APA.
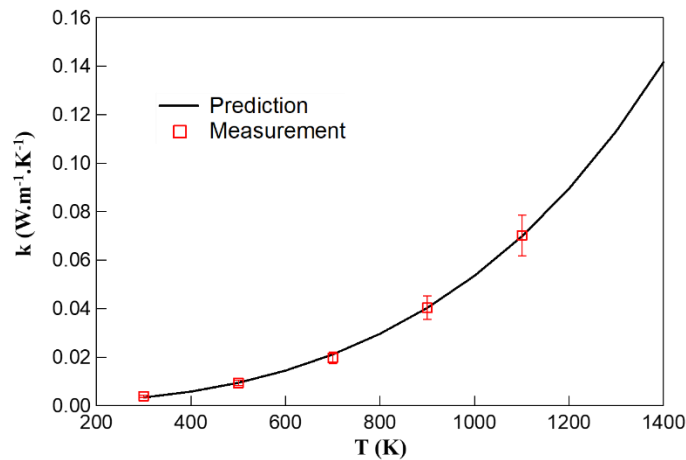

Figure 37. Comparison of predicted and measured thermal conductivity of APA in vacuum. (Measurements using three-point step heating method by a commercial laboratory, Ref. 54)

33

Using the low-pressure thermal conductivity from Eq. (30) and pore size of 8.16×10^{-5} m, one can calculate thermal conductivity of APA with a nominal density of 98.4 kg.m^{-3} at various pressures and temperatures and in various gases. The low-pressure thermal conductivity can be further broken down into its radiation and solid conduction components according to Eq. (26), with the unknown parameters estimated using genetic algorithm optimization applied to cryogenic and high-temperature thermal conductivity data in vacuum, with the parameter estimates provided in Eqs. (33.a and 33.b). The major sources of uncertainty for the latter approach are the cryogenic thermal diffusivity measurements and the thermal conductivity of bulk material at cryogenic temperatures.

8.3. OFI

The next sample studied was opacified fibrous insulation (OFI) which consists of silicon carbide opacifiers embedded in an alumina-based fibrous insulation for further attenuating the radiation mode of heat transfer. The OFI sample fiber volume fraction was estimated to be 0.0311. The variation of OFI integrated thermal conductivity with T_i at non-dimensional heights of 1, 0.857, 0.572, 0.285, and 0.143 at a pressure of 0.001 torr is shown in Figure 38. The water-cooled plate temperatures for these tests varied between 287.2 K and 291.2 K, with an average temperature of 289.1 K ±3.8 K for a 95% confidence interval. The error bars, used for the L_i/L =1 data represent the experimental uncertainty. The total uncertainties varied within 8.8%
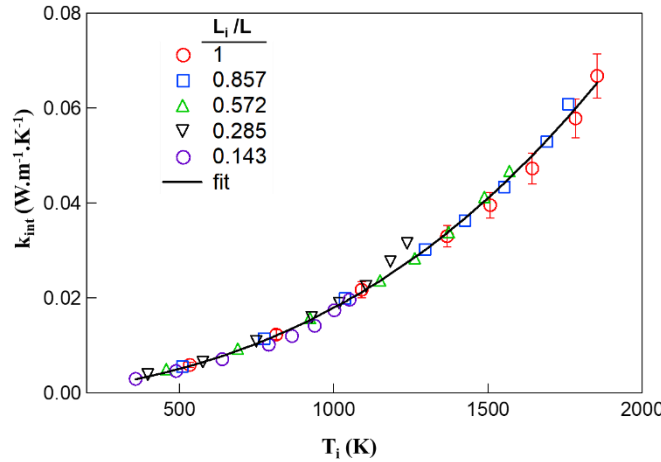

Figure 38. Variation of OFI integrated thermal conductivity with internal sample temperatures in vacuum.

at T_H of 534.1 K and 6.9% at T_H of 1853.6 K. The k_{int} values for the various L_i/L data collapse to a single curve as shown in the figure. A regression analysis was used in conjunction with Eq. (21) and the data in Figure 38 to obtain the unknown coefficients for the low-pressure thermal conductivity of OFI for LaRC Test 603, resulting in

$$k_{LP} = -2.386 \times 10^{-3} + 7.818 \times 10^{-6}T + 2.075 \times 10^{-8}T^2 + 1.654 \times 10^{-11}T^3 \qquad (34)$$

with k_{LP} in W.m^{-1}.K^{-1} and T in K. The low-pressure thermal conductivity of OFI over the temperature range of 290 K to 1850 K for the specific composition of LaRC Test 603 OFI sample is defined by Eq. (34) and other compositions of OFI can have different k_{LP} values. It is assumed that the total uncertainty of k_{LP} and thermal conductivity at higher pressures for OFI is equal to the maximum total uncertainty calculated for k_{int}, which is 8.8%. The comparison of $\rho.k_{LP}$ of OFI and APA is shown in Figure 39, where APA k_{LP} data above 1700 K are extrapolated data. OFI exhibits lower $\rho.k_{LP}$ compared to APA, with the difference increasing with increasing temperature, demonstrating OFI's capability to significantly reduce radiation thermal conductivity at high temperatures compared to alumina fibrous insulation samples. The ratio of OFI to APA $\rho.k_{LP}$ varies between 0.47 to 0.8 over the entire temperature range, with the ratio decreasing with increasing temperature. At 1700 K, the ratio is 0.509. Since the OFI test sample and APA have similar

34

densities, 99.2 kg.m^{-3} for OFI and 98.4 kg.m^{-3} for APA, it can be concluded that OFI has half the low-pressure thermal conductivity of APA for $T \geq 1700$ K.
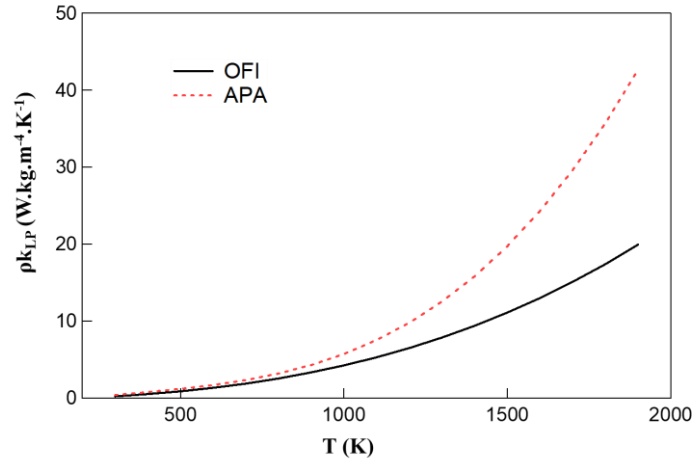
Figure 39. Comparison of variation of OFI and APA $\rho.k_{LP}$ with temperature in vacuum (densities of 99.2 kg.m^{-3} and 98.4 kg.m^{-3} for OFI and APA, respectively).

Because of presence of opacifier additives in the fiber matrix, Eq. (13) cannot be used to estimate the gas conduction pore size for OFI. A plot showing the variation of k_{int} versus pressure obtained from temperatures at non-dimensional heights of 1, 0.857, 0.572, 0.285, and 0.143 for T_H of 1360 K is shown in Figure 40. This data was used to estimate the gas conduction characteristic length using an equal search interval optimization routine. For various estimates of κ, k_g was calculated from Eq. (8), added to k_{LP} from Eq. (34), then integrated using Eq. (19) for each of the corresponding sets of input data (T_i, T_c, P) to estimate k_{int}. A value of κ was sought that would minimize the root sum square difference between the estimated and measured k_{int} values from Figure 40. Using this procedure, the OFI pore size was determined to be 1.38×10^{-4} m, which is for the specific OFI composition used for this study, and cannot be applied to other OFI compositions. Using this κ and k_{LP} from Eq. (34), thermal conductivity data for various temperatures and pressures in dry air were calculated and presented in Table 6 in the Appendix.
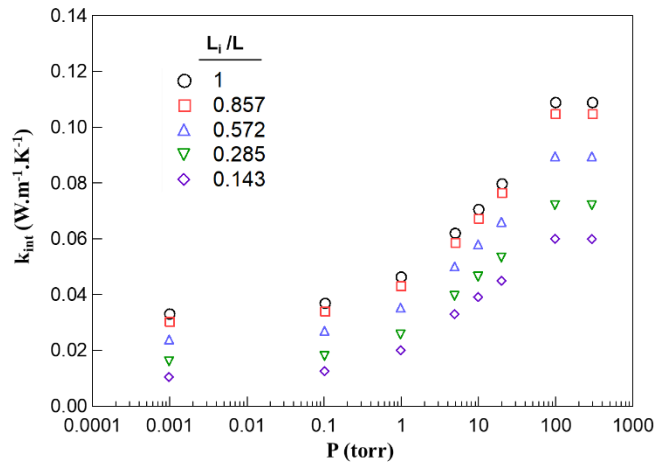
Figure 40. Variation of OFI integrated thermal conductivity with static pressure in nitrogen for $T_H = 1360$ K.

The OFI data show how opacifier use in a fibrous insulation sample can significantly reduce the radiation mode of heat transfer in the composite insulation. No attempt was made to develop a detailed model for

OFI due to the complexity of modeling the combined contributions of fibers and opacifiers to solid conduction and radiation heat transfer modes.

8.4. APA2-AS

Before discussing the APA2-AS test results, a discussion of the influence of pore size on thermal conductivity of insulation samples is provided. Suppose an insulation has low-pressure thermal conductivity equal to that of APA from Eq. (30). Thermal conductivity data were generated for this insulation as a function of pressure at a constant temperature of 1400 K with pore sizes of 1×10^{-4} m, 1×10^{-5} m, 1×10^{-6} m, and 1×10^{-7} m, with the results shown in Figure 41. All the data sets share the same k_{LP}, so the various data sets have equal thermal conductivity values up to approximately 0.1 torr. For pore size of 1×10^{-4} m, gas conduction contribution starts around 0.1 torr, and by 200 torr reaches its continuum value. For pore size of 1×10^{-5} m, gas conduction contribution begins around 1 torr, and by 760 torr it has not reached its full continuum value. The thermal conductivity values above 0.1 torr are lower for κ of 1×10^{-5} compared to κ of 1×10^{-4}. The same general pattern occurs as the pore size reduces further. Gas conduction contribution starts around 10 torr and 100 torr for κ of 1×10^{-6} m and 1×10^{-7} m, respectively, and does not reach the continuum value at 760 torr for either case. This behavior is typical for microporous and aerogel insulation samples, which have pore sizes of 1×10^{-6} m or lower. Aerogels delay the onset of gas conduction till higher pressure values ($P > 10$ torr), and do not reach continuum gas conduction levels at 760 torr. Aerogels may have lower thermal conductivities compared to standard fibrous insulation samples at pressures above 1 torr. However, additional information will be provided later in this section to show that aerogels do not provide any advantage in vacuum conditions ($P < 0.1$ torr).

APA2-AS is fabricated by embedding aluminosilicate aerogels in APA felt. The APA2-AS sample fiber volume fraction was estimated to be 0.0479. The variation of calculated APA2-AS integrated thermal conductivity with T_i at various non-dimensional heights of 1, 0.75, 0.5, and 0.25 at a pressure of 0.001 torr for LaRC Test 612 is shown in Figure 42. For the tests at 0.001 torr, the water-cooled plate temperature
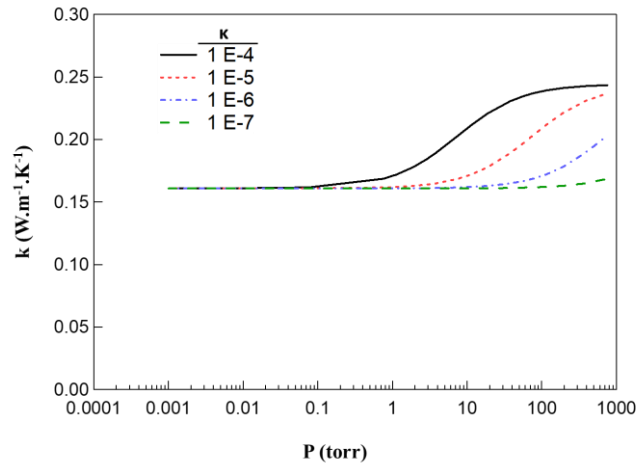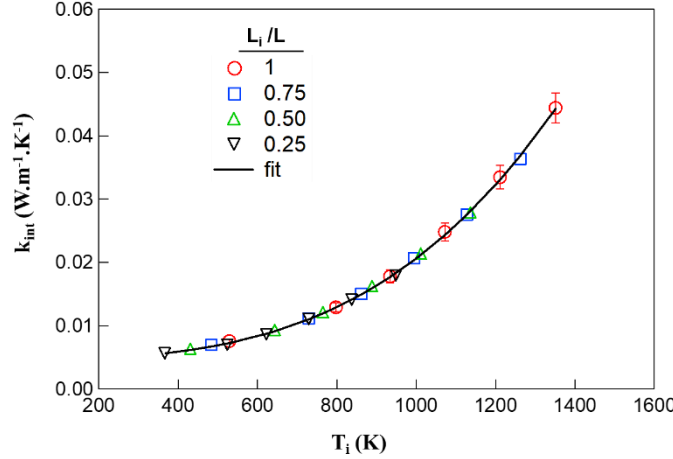

**Figure 41. Influence of pore size on thermal conductivity in dry air.**

Figure 42. Variation of APA2-AS integrated thermal conductivity with internal sample temperatures in vacuum.

varied between 284.4 K and 288 K, with an average temperature of 285.7 K ±2.7 K for a 95% confidence interval. The error bars, used for $L_i/L = 1$ data represent the experimental uncertainty. The total uncertainties varied between 5.1% and 5.8% over the temperature range of tests. The k_{int} values for the various L_i/L data collapse to a single curve, as shown in the figure. A regression analysis was used in conjunction with Eq. (21) and the data in Figure 42 to obtain the unknown coefficients for the low-pressure thermal conductivity of APA2-AS, resulting in

$$k_{LP} = 2.581 \times 10^{-3} + 1.288 \times 10^{-5}T - 3.534 \times 10^{-8}T^2 + 7.441 \times 10^{-11}T^3 \qquad (35)$$

with k_{LP} in W.m^{-1}.K^{-1} and T in K. Eq. (35) provides the low-pressure thermal conductivity of APA2-AS over the temperature range of 284 K and 1350 K. It is assumed that the total uncertainty of k_{LP} and thermal conductivity at higher pressures for APA2-AS is equal to the maximum total uncertainty calculated for k_{int}, which is 5.8%. A comparison of the product of density and low-pressure thermal conductivity ($\rho.k_{LP}$) for APA2-AS (148.2 kg.m^{-3}) and APA (98.4 kg.m^{-3}) is shown in Figure 43. At low pressure, APA has lower $\rho.k_{LP}$ compared to APA2-AS, with the difference increasing with increasing temperature. The presence of aerogel particles (30% be weight) in APA felt may increase the solid conduction mode and also adversely influence the overall radiative performance. APA has 32% to 45% lower $\rho.k_{LP}$ compared to APA2-AS between 800 K and 1400 K. Since the difference in $\rho.k_{LP}$ increases with increasing temperature, radiation must be the main cause for the difference.

Eq. (13) cannot be used to estimate the gas conduction pore size for APA2-AS, since the equation is only valid for fibrous insulation samples without additives. The variation of k_{int} versus pressure for APA2-AS obtained from temperature measurements at non-dimensional heights of 1, 0.75, 0.5, and 0.25 for a hot-side setpoint temperature of 1210 K is shown in Figure 44. This data was used to estimate the pore size using an equal search interval optimization routine, similar to the procedure explained previously for OFI. The APA2-AS pore size was determined to be 2.985×10^{-7} m, verifying that the presence of aluminosilicate aerogels in APA results in very low pore size, orders of magnitude lower than typical fibrous insulation (1.29×10^{-4} m for ZYF and 8.16×10^{-5} m for APA). Thermal conductivity data for APA2-AS were calculated as a function of temperature for various pressures in dry air and presented in Table 7 in the Appendix.

37
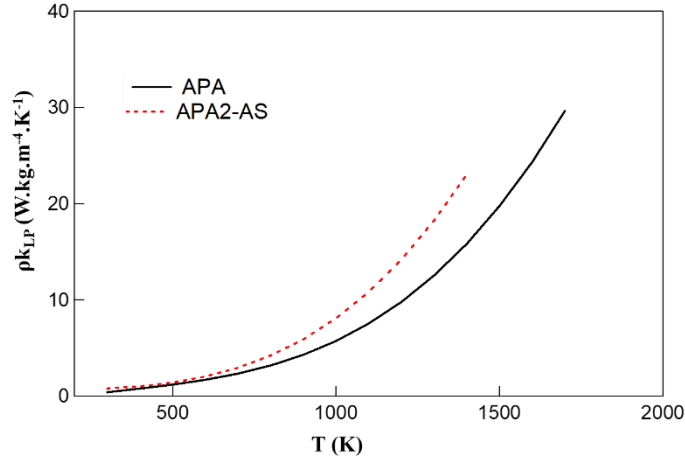
Figure 43. Comparison of variation of APA2-AS and APA $\rho.k_{LP}$ with temperature in vacuum (densities of 98.4 kg.m^{-3} and 148.2 kg.m^{-3} for APA and APA2-AS, respectively).

To compare pressure dependency of APA2-AS and APA, a plot of the product of density and thermal conductivity ($\rho.k$) versus pressure for the two insulation samples at a temperature of 1000 K is shown in Figure 45. APA exhibits standard fibrous insulation behavior. The thermal behavior below 0.1 torr is due to radiation and solid conduction. Gas conduction contribution starts around 0.1 torr, and its contribution increases with increasing pressure until 100 torr, after which the gas conduction contribution stays relatively constant with increasing pressure. For APA2-AS, gas conduction contribution starts above 40 torr, and does not reach its constant continuum value at 760 torr. APA has lower $\rho.k$ compared to APA2-AS up to 3 torr, but above 3 torr, APA has higher $\rho.k$ compared to APA2-AS. So, use of aerogels in fibrous insulation makes the resulting compound insensitive to pressure up to 40 torr, and less sensitive to pressure above 40 torr. The thermal behavior of APA2-AS below 3 torr is not as good as APA, proving that there is no advantage in using aerogels at very low pressures. The thermal behavior of APA2-AS above 3 torr is better
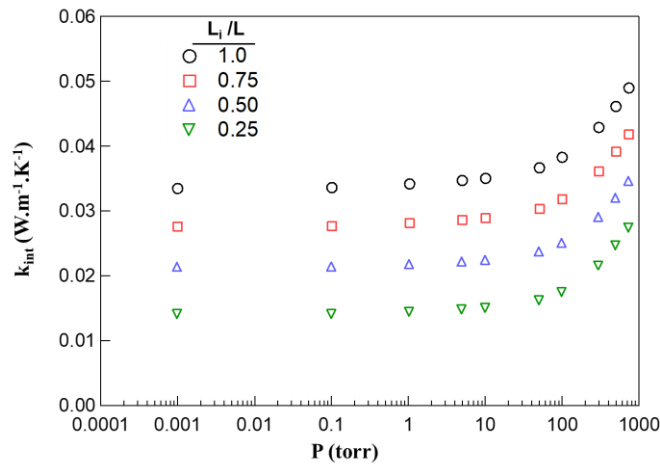
Figure 44. Variation of APA2-AS integrated thermal conductivity with static pressure in nitrogen for $T_H = 1210$ K.

than APA, showing the benefits of reducing gas conduction mode of heat transfer at higher pressures. It should be noted that the specific values cited here are for data at 1000 K shown in Figure 45, and any

38

changes in temperature could cause a change in the values and the crossover point, but the trends will stay the same.
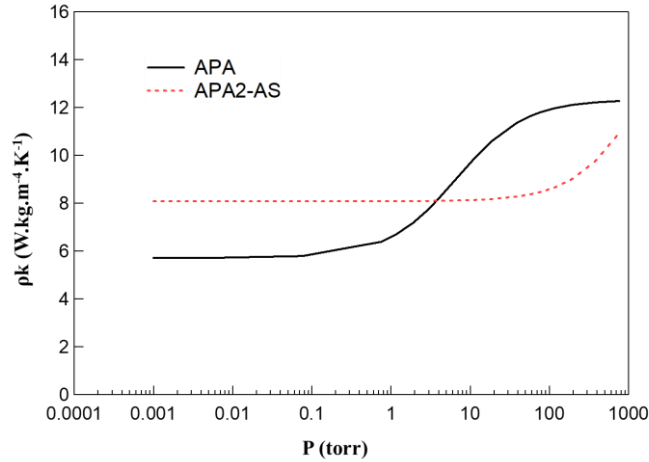
Figure 45. Comparison of variation of APA2-AS and APA $\rho.k$ with static pressure at 1000 K in dry air.

It was shown that incorporation of aerogels in a fibrous insulation can attenuate the gas conduction mode of heat transfer. No attempt was made to develop a detailed model for APA2-AS due to the complexity of modeling the combined contributions of fibers and aerogels to solid conduction and radiation modes of heat transfer.

8.5. Saffil

The tested Saffil samples did not have any internal thermocouples, so the integrated thermal conductivities had been calculated only using the hot-side temperature. The variation of calculated integrated thermal conductivities with T_H at 0.001 torr for samples with densities of 24.2 kg.m^{-3}, 48 kg.m^{-3}, and 96.1 kg.m^{-3} are provided in Figure 46. The water-cooled plate temperatures varied between 295.6 K and 306.5 K for the test with sample density of 24.2 kg.m^{-3}, with an average temperature of 299.2 K ±8.88 K for a 95% confidence interval. For the tests with sample densities of 48 kg.m^{-3} and 96.1 kg.m^{-3} the average water-cooled plate temperatures were 290.1 K ±10.7 K and 286.4 K ±6.1 K for a 95% confidence interval,
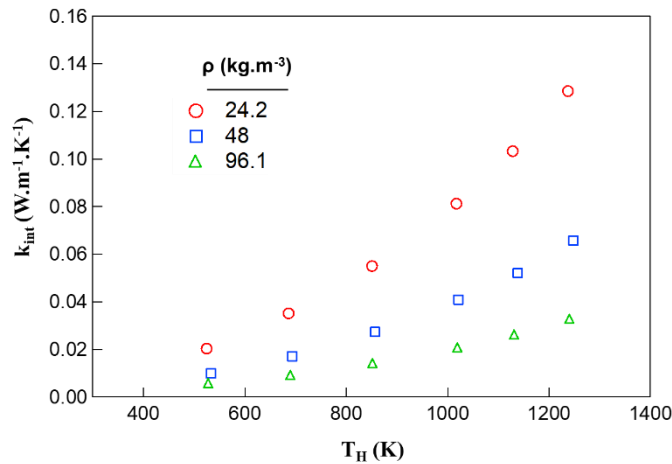
Figure 46. Variation of Saffil integrated thermal conductivity with hot-side temperature in vacuum for various sample densities.

respectively. Uncertainty estimates for the 24 kg.m^{-3} sample varied between 5.5% and 9.7% (Ref. 40). A regression analysis was used in conjunction with Eq. (21) and each set of data in Figure 46 to obtain the unknown coefficients for the low-pressure thermal conductivity of Saffil at the three densities

$$k_{LP} = -2.316 \times 10^{-2} + 9.484 \times 10^{-5}T - 5.094 \times 10^{-8}T^2 + 1.792 \times 10^{-10}T^3 \quad (24.2 \text{ kg.m}^{-3}) \quad (36.a)$$

$$k_{LP} = -9.591 \times 10^{-3} + 3.908 \times 10^{-5}T - 1.920 \times 10^{-8}T^2 + 9.121 \times 10^{-11}T^3 \quad (48 \text{ kg.m}^{-3}) \quad (36.b)$$

$$k_{LP} = -3.850 \times 10^{-3} + 2.017 \times 10^{-5}T - 1.467 \times 10^{-8}T^2 + 4.892 \times 10^{-11}T^3 \quad (96.1 \text{ kg.m}^{-3}) \quad (36.c)$$

with k_{LP} in W.m^{-1}.K^{-1} and T in K. These equations provide the low-pressure thermal conductivity of Saffil at the specified densities over the temperature range of 300 K and 1400 K, and are shown in Figure 47.
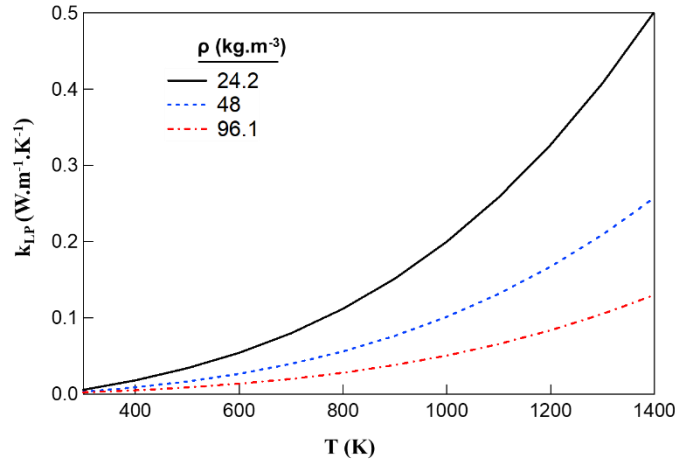
Figure 47. Variation of Saffil low-pressure thermal conductivity with temperature for various sample densities.

It is assumed that the total uncertainty of k_{LP} and thermal conductivity at higher pressures for Saffil at various densities is equal to the maximum total uncertainty calculated for k_{int} at 24 kg.m^{-3}, which is 9.7%. A comparison of the product of density and low-pressure thermal conductivity ($\rho.k_{LP}$) for the three Saffil samples is shown in Figure 48. The 9.7% uncertainty estimates shown are for the 48 kg.m^{-3} data. The three sets of $\rho.k_{LP}$ data match each other. In vacuum, $\rho.k_{LP}$ stays constant for any insulation at various densities, as long as the overall insulation fiber morphology stays consistent between the samples. This implies that k_{LP} can be calculated for the insulation at any density (any practically feasible density) from the known data at a specific density

$$\rho_1 k_{LP,1} = \rho_2 k_{LP,2} \tag{37}$$

This equation only applies in vacuum and does not hold at higher pressures. Once the unknown $k_{LP,1}$ is determined from the known $k_{LP,2}$ using Eq. (37), the pore size is calculated from Eq. (13) using ρ_1, then the gas conduction contribution can be calculated from Eqs. (8-13). The implication stemming from Eq. (37) is that one does not always need to develop and use the detailed model to get thermal properties of an insulation at different densities. However, the detailed model is useful because it can provide the specific contributions of solid conduction and radiation modes of heat transfer in the insulation.
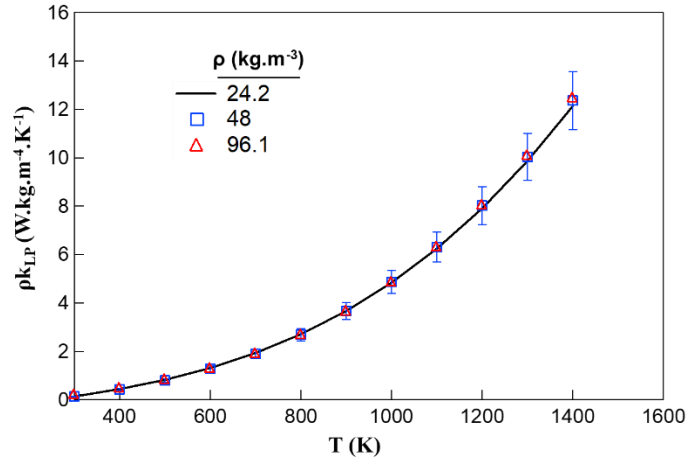
Figure 48. Variation of Saffil $\rho.k_{LP}$ with temperature for various sample densities in vacuum.

The thermal conductivity of a custom-made Saffil at a density of 144.5 kg.m^{-3} had been measured in nitrogen at pressures of 5×10^{-3} torr, 1 torr, and 760 torr for temperatures between 296 K and 1089 K using the three-point step heating technique (Ref. 23) by a commercial laboratory (Ref. 55). The k_{LP} data for a density of 48 kg.m^{-3} from Eq. (36.b) was used to calculate k_{LP} at 144.5 kg.m^{-3}, and then gas conduction contribution was calculated from Eqs. (8-13) to infer thermal conductivity at higher pressures in nitrogen at a density of 144.5 kg.m^{-3}. The comparison of predicted and measured thermal conductivities for this sample is provided in Figure 49. The measurements are shown as symbols with their reported ±12% measurement uncertainty by the commercial laboratory (Ref. 55). The solid lines are the predictions. Close agreement can be observed at all pressures and temperatures; the difference between predicted and measured values varied between 0.4% and 23.8% over the pressure and temperature range, with the difference generally decreasing with increasing temperature, and with a RMSD of 11.8%.

Using a mean fiber diameter of 4.5 μm, and an estimated fiber volume fraction of 0.0147, the pore size for Saffil at a density of 48 kg.m^{-3} was determined to be 2.43×10^{-4} m. Using this pore size, thermal conductivity data for Saffil at 48 kg.m^{-3} were calcualted as a function of temperature for various pressures in dry air and presented in Table 8 in the Appendix. Thermal conductivity data for Saffil at 96 kg.m^{-3} in dry air were also calculated and presented in Table 9 in the Appendix. The comparison of $\rho.k$ for Saffil samples at densities of 24, 48, and 96 kg.m^{-3} at 7.6 torr pressure in air is shown in Figure 50. Unlike the $\rho.k$ data in vacuum in Figure 48, where data at different densities matched each other, in the presence of gas conduction the $\rho.k$ data at higher pressures vary with sample density. The lower the density, the lower the $\rho.k$ values. As density increases, the fiber volume fraction increases, causing the pore size to decrease, according to Eq. (13), resulting in lower gas thermal conductivity and lower total thermal conductivity. However, the decreases in total thermal conductivity do not necessarily lead to lower $\rho.k$. Consequently, for any insulation at various densities when the fiber diameter and fiber morphology do not vary with density, the product of $\rho.k$ is identical in vacuum but varies at elevated pressures where gas conduction is present.
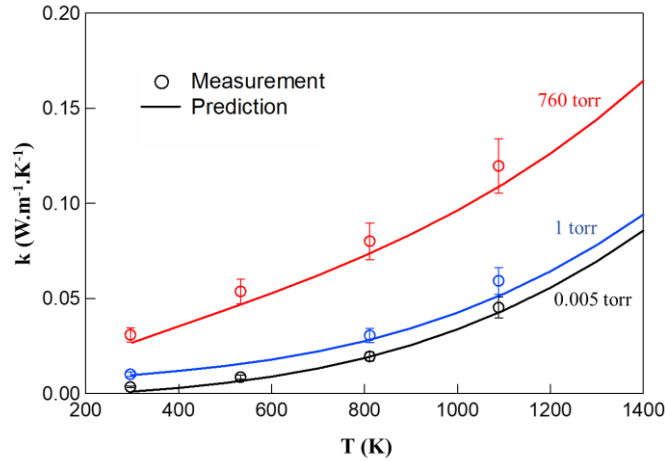
Figure 49. Comparison of predicted and measured thermal conductivity of Saffil at 144.5 kg.m⁻³ at three static pressures in nitrogen. (Measurements using three-point step heating method by a commercial laboratory, Ref. 55).
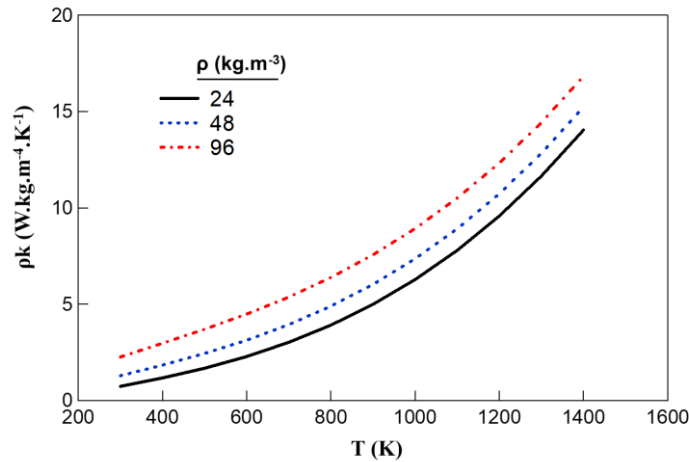
Figure 50. Variation of Saffil $\rho.k$ with temperature in dry air at static pressure of 7.6 torr for various sample densities.

Some of the pertinent data for the various insulation materials studied here are summarized in Table 10 in the Appendix.

9. Optimum Insulation Layup

To determine optimum insulation layups for a specific application, one needs to study the relative importance of the various heat transfer modes at various pressures and temperatures. The ratio of component (solid conduction, gas conduction, radiation) thermal conductivity to total thermal conductivity as a function of temperature at pressures of 0.001 torr, 5 torr, and 50 torr for APA are shown in Figure 51. The listed pressures correspond to static pressures at altitudes of 93 km, 35.8 km, and 18.8 km, respectively. The sum of the three component ratios at each temperature equals unity.

At 0.001 torr pressure (Figure 51.a), solid conduction is 18.7% of total thermal conductivity at 300 K, but rapidly decreases with increasing temperature, and falls below 1% above 800 K. Gas conduction is negligible at all temperatures at 0.001 torr, starts at 0.3% at 300 K, and drops below 0.1% above 500 K.

42

Radiation starts at 81% of total thermal conductivity at 300 K, rapidly rises with increasing temperature, and exceeds 99% above 800 K. At this low pressure, radiation is the dominant mode of heat transfer at all temperatures. At 5 torr pressure (Figure 51.b) solid conduction is 3% of total thermal conductivity at 300 K and falls below 1% above 600 K. Gas conduction is 83.8% of total thermal conductivity at 300 K, and decreases with increasing temperature, and equals 9.1% at 1700 K. Radiation starts at 13.2% of total thermal conductivity at 300 K, and increases with increasing temperature, reaching 90.8% at 1700 K. At 5 torr pressure solid conduction is essentially negligible, and gas conduction and radiation are both important. Gas conduction is the dominant mode at lower temperatures, while radiation is dominant at higher temperatures. The crossover point where gas conduction and radiation are equal is approximately 700 K. Similar patterns are observed with the 50 torr pressure data shown in Figure 51.c. Solid conduction is 2.3% of total thermal conductivity at 300 K and falls below 1% at 500 K. Gas conduction varies between 87.5% at 300 K and 20.9% at 1700 K, while radiation varies between 10.2% at 300 K and 79.1% at 1700 K. Radiation and gas conduction modes equal at approximately 1000 K. A pressure increases from 5 torr to 50 torr, the relative importance of gas conduction increases, and the crossover point changes from 700 K to 1000 K.

Based on the data presented in Figures 51.a-c, general optimized insulations layups can be considered. For applications where insulation is used at very low pressures such as deep space or hypersonic cruise flights at high altitudes, radiation is the dominant mode of heat transfer. It would be beneficial to use an insulation that attenuates the radiation mode of heat transfer. It could be either radiation attenuating insulation throughout the entire thickness or a mixed layup with the radiation attenuating insulation used closer to the outer mold line (hot-side boundary), and regular fibrous insulation used closer to the inner mold line (cold side boundary). The relative thicknesses of each insulation layer can be determined using optimization methods in conjunction with thermal analysis for the specific aeroheating profile. For applications at higher pressures, radiation and gas conduction are the dominant modes, with radiation being more dominant closer to the outer mold line and gas conduction closer to the inner mold line. For these cases, a radiation attenuating insulation should be used closer to the outer mold line, and a gas conduction attenuating insulation should be used closer to the inner mold line. The insulation layup could also use regular fibrous insulation between the radiation and gas conduction attenuating insulation layers. Utilizing optimization and thermal analysis, the relative thicknesses of the various insulation layers can be determined for the specific application. A typical spacecraft re-entry experiences the full range of pressures from very low pressures at high altitudes to higher pressures as a spacecraft descends through the atmosphere, so the latter optimum insulation layup would be useful. Typical insulation optimization is based on either minimizing mass or minimizing thickness due to volume constraints.
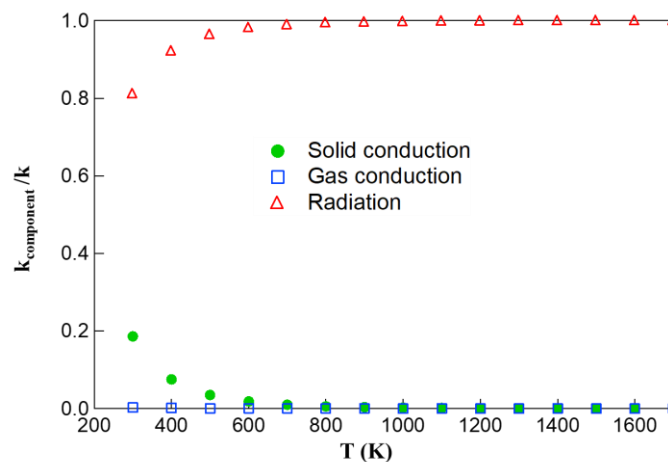
a)
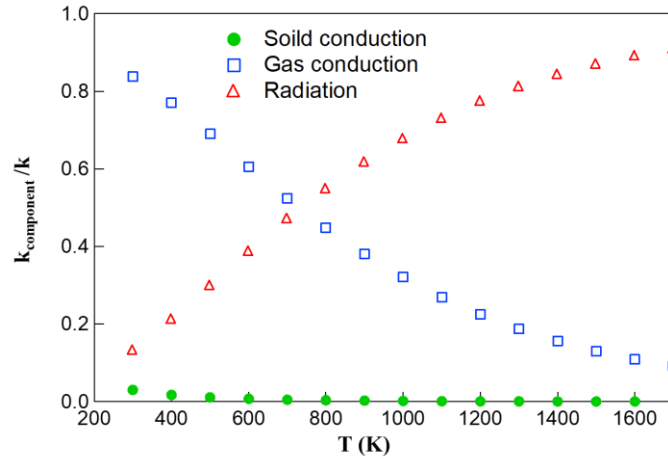
b)
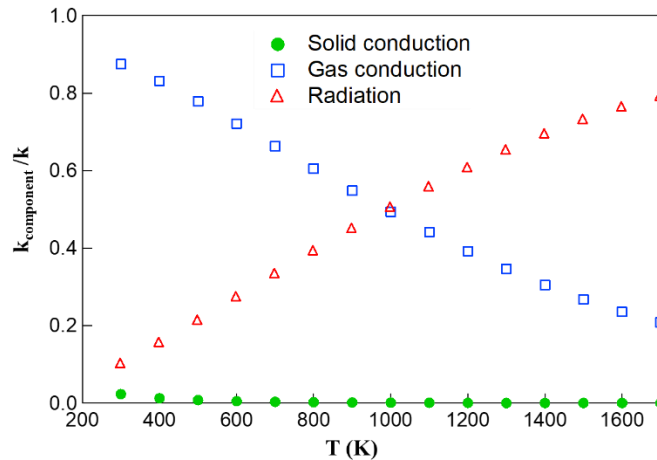
c)

Figure 51. Variation of ratio of component thermal conductivity to total thermal conductivity with temperature for APA in dry air for static pressures of: a) 0.001 torr, b) 5 torr, c) 50 torr.

10. Concluding Remarks

Testing and modeling of heat transfer in high-temperature, high-porosity, flexible refractory ceramic fibrous insulation felts was investigated. A semi-empirical model that requires inverse methods and steady-state thermal test data to infer some of the required model parameters was further developed in this study and applied to various insulation samples for temperatures between 300 K and 1900 K. The steady-state thermal test setup at NASA Langley Research Center with the recent modifications to increase its testing capability from 1400 K to 1900 K was presented. Test data and corresponding thermal models for three high-temperature flexible refractory ceramic fibrous insulations were presented. Furthermore, test data and thermal models on two fibrous insulation samples containing additives to further suppress either radiation or gas conduction modes of heat transfer were presented. The significance of various heat transfer modes in these insulation samples was discussed. General guidelines for optimum insulation layups were discussed.

44

References

1. Hager, N. E., and Steere, R. C., "Radiant Heat Transfer in Fibrous Thermal Insulation," *Journal of Applied Physics*, Vol. 38, No. 12, 1967, pp. 4663-4668. doi.org/10.1063/1.1709200

2. Bankvall, C., "Heat Transfer in Fibrous Materials," *Journal of Testing and Evaluation*, Vol. 1, No. 3, 1973, pp. 235-243.

3. Lee, S. C., and Cunnington, G. R., "Conduction and Radiation Heat Transfer in High-Porosity Fiber Thermal Insulation," *Journal of Thermophysics and Heat Transfer*, Vol. 14, No. 2, 2000, pp. 121-136. doi.org/10.2514/2.6508

4. Kennard, E. H., *Kinetic Theory of Gases*, McGraw-Hill, New York, 1938, pp. 163-179, 290-318.

5. Marcussen, L., "Prediction of Effective Thermal Conductivity for Fibrous Media," *Thermal Conductivity*, 19, edited by David Yarbrough, 1985, Plenum Press, pp. 75-84.

6. Daryabeigi, K., Cunnington, G. R., and Knutson, J. R., "Combined Heat Transfer in High-Porosity High-Temperature Fibrous Insulations: Theory and Experimental Validation," *Journal of Thermophysics and Heat Transfer*, Vol. 25, No. 4, October–December 2011, pp. 536-546. doi.org/10.2514/1.T3616

7. Matthews, L. K., Viskanta, R., and Incropera, F. P., "Combined Conduction and Radiation Heat Transfer in Porous Materials Heated by Intense Solar Radiation," *Journal of Solar Energy Engineering*, Vol. 107, No. 1, 1985, pp. 29-34. doi.org/10.1115/1.3267649

8. Tong, T. W., and Tien, C. L., "Radiative Heat Transfer in Fibrous Insulations-Part I: Analytical Study," *Journal of Heat Transfer*, Vol. 105, No. 1, 1983, pp. 70-75. doi.org/10.1115/1.3245561

9. Tong, T. W., Yang, Q. S., and Tien, C. L., "Radiative Heat Transfer in Fibrous Insulations-Part II: Experimental Study," *Journal of Heat Transfer*, Vol. 105, No. 1, 1983, pp. 76-81. doi.org/10.1115/1.3245562

10. Houston, R. L., and Korpela, S. A, "Heat Transfer through Fiberglass Insulations," *Proceedings of the 7th International Heat Transfer Conference*, Vol. 2, Hemisphere, Washington, DC, 1982, pp. 499–504. doi.org/10.1615/IHTC7.4040

11. Lee, S. C., "Radiative Transfer through a Fibrous Medium: Allowance for Fiber Orientation," *Journal of Quantitative Spectroscopy and Radiative Transfer*, Vol. 36, No. 3, 1986, pp. 253-263. doi.org/10.1016/0022-4073(86)90073-7

12. Lee, S. C., "Scattering Phase Function for Fibrous Media," *International Journal of Heat and Mass Transfer*, Vol. 33, No. 10, 1990, pp. 2183-2190. doi.org/10.1016/0017-9310(90)90119-F

13. Lee, S. C., "Radiation Heat Transfer through Carbon Fiber Materials: Experiment vs Theory," *Journal of Thermophysics and Heat Transfer*, Vol. 33, No. 2, pp. 370-377, 2019. doi.org/10.2514/1.T5531

14. Carvajal, S. A., Garboczi, E. J., and Zarr, R. R., "Comparison of Models for Heat Transfer in High-density Fibrous Insulation," *Journal of Research National Institute of Standards and Technology*, Vol. 124, No. 124010, pp. 1-21, 2019. doi.org/10.6028/jres.124.010

15. Carvajal, S. A., Daryabeigi, K., and Ramirez, J. H., "Predictive Radiation Heat Transfer Modeling in Fibrous Insulation at High Temperatures," *International Journal of Thermal Sciences*, Vol. 198, April 2024. doi.org/10.1016/j.ijthermalsci.2024.108897

16. ASTM Standard C 177, "Standard Test Method for Steady-State Heat Flux Measurements and Thermal Transmission Properties by Means of the Guarded-Hot-Plate Apparatus," ASTM International, West Conshohocken, PA, 2019. doi.org/10.1520/C0177-19

17. ASTM Standard C 518, "Standard Test Method for Steady-State Thermal Transmission Properties by Means of the Heat Flow Meter Apparatus," ASTM International, West Conshohocken, PA, 2021. doi.org/10.1520/C0518-21

18. Flynn, D. R., "A Radial-flow Apparatus for Determining the Thermal Conductivity of Loose-Fill Insulations to High Temperatures," *Journal of Research of the National Bureau of Standards-C. Engineering and Instrumentation*, Vol. 67C, No. 2, April-June 1963, pp. 129-137.

19. Zarr, R. R., Wu, J., and Liu, H, "NIST-NPL Bilateral Comparison of Guarded-Hot-Plate Laboratories from 20°C to 160°C," NIST Technical Note 2059, January 2020. doi.org/10.6028/NIST.TN.2059

20. https://www.kratosdefense.com/about/divisions/defense-and-rocket-support-services/sre/thermal-testing-of-materials

21. ASTM E1225-20, "Standard Test Method for Thermal Conductivity of Solids by Means of the Guarded-Comparative-Longitudinal Heat Flow Technique," ASTM International, West Conshohocken, PA, 2020. doi.org/10.1520/E1225-20

22. ASTM-E1461, "Standard Test Method for Thermal Diffusivity by the Flash Method," ASTM International, West Conshohocken, PA, 2013. doi.org/10.1520/E1461

23. Gembarovic, J., and Taylor, R. E., "A Method for Thermal Diffusivity Determination of Thermal Insulators," *International Journal of Thermophysics,* Vol. 28, 2007, pp. 2164-2175. doi:10.1007/s10765-007-0279-7

24. ASTM E1269-11, "Standard Test Method for Determining Specific Heat Capacity by Differential Scanning Calorimetry," ASTM International, West Conshohocken, PA, 2011. doi.org/10.1520/E1269

25. Daryabeigi, K., Blosser, M. L., Geouge, W. D., and Cheatwood, J. S., "A Simple Transient Thermal Test Assembly for Insulation Materials," NASA TM- 2019-220249, 2019.

26. Kurz, E., and Daryabeigi, K., "Thermal Conductivity Estimation from Transient Test Data with Embedded Thermocouples using Genetic Algorithms," NASA TM-20210014330, May 2021.

27. Daryabeigi, K., Knutson, J. R., and Cunnington, G. R., "Reducing Thermal Contact Resistance for Rigid Insulation Thermal Measurements," *Journal of Thermophysics and Heat Transfer*, Vol. 26, No. 1, January-March 2012, pp. 172-175. doi.org/10.2514/1.T3788

28. Daryabeigi, K., Cunnington, G. R., and Knutson, J. R. "Heat Transfer Modeling for Rigid High-Temperature Fibrous Insulation" *Journal of Thermophysics and Heat Transfer*, Vol. 27, No. 3, July-September 2013, pp. 414-421. doi.org/10.2514/1.T3998

29. Stark, C., and Fricke, J., "Improved Heat-Transfer Models for Fibrous Insulations," *International Journal of Heat and Mass Transfer*, Vol. 36, No. 3, 1993, pp. 617-625. doi.org/10.1016/0017-9310(93)80037U

30. Daryabeigi, K., "Heat Transfer in High-Temperature Fibrous Insulation," *Journal of Thermophysics and Heat Transfer*, Vol. 17, No. 1, 2003, pp. 10-20. doi.org/10.2514/2.6746

31. Sparrow, E. M., and Cess, R. D, *Radiation Heat Transfer*, Hemisphere Publishing Corp, Washington, 1978.

32. Pettyjohn, R. R., "Thermal Conductivity Measurements on a Fibrous Insulation Material," *Proceedings of the Seventh Conference on Thermal Conductivity*, NBS Special Publication 302, Edited by D. R. Flynn and B. A. Peavy Jr., U.S. Government Printing Office, Washington, DC, 1968, pp. 729-736.

33. Touloukian, Y. S., Powell, R. W., Ho, C. Y., and Klemens, P. G., *Thermal Conductivity Nonmetallic Solids*, Vol. 2, Thermophysical Properties of Matter, IFI/Plenum, New York-Washington, 1970.

34. Caren, R. P., "Radiation Heat Transfer from a Metal to a Finely Divided Particulate Medium," *Journal of Heat Transfer,* Vol. 91, 1969, pp. 154-156. doi.org/10.1115/1.3580074

35. Touloukian, Y. S., Liley, P. E., and Saxena, S. C., *Thermal Conductivity, Nonmetallic Liquids and Gases*, Vol. 3, Thermophysical Properties of Matter, IFI/Plenum, New York-Washington, 1970.

36. Touloukian, Y. S., and Makita, T., *Specific Heat, Nonmetallic Liquids and Gases*, Vol. 6, Thermophysical Properties of Matter, IFI/Plenum, New York-Washington, 1970.

37. Touloukian, Y. S., Saxena, S. C., and Hestermans P., *Viscosity*, Vol. 11, Thermophysical Properties of Matter, IFI/Plenum, New York-Washington, 1970.

38. White, F. M., *Viscous Fluid Flow*, McGraw-Hill, New York, 1974.

39. Verschoor, J. D., and Greebler, P., "Heat Transfer by Gas Conduction and Radiation in Fibrous Insulations," *Transactions of the American Society of Mechanical Engineers*, Vol. 74, No. 8, 1952, pp. 961-968. doi.org/10.1115/1.4015979

40. Daryabeigi, K., "Effective Thermal Conductivity of High Temperature Insulations for Reusable Launch Vehicles," NASA TM-1999-208972, February 1999.

41. Goldstein, H. E., Leiser, D. B., Smith, M., and Stewart, D., "Opacified Silica Reusable Insulation (RSI) for Thermal Protection of the Space Shuttle Orbiter," ed. By Mirkovich, V.V., *Thermal Conductivity,* 15, Springer, MA, 1977, pp. 335-34. doi.org/10.1007/978-1-4615-9083-5_40

42. Grunert, W. E., Notaro, F., and Reid, R. L., "Opacified Fibrous Insulation," AIAA Paper 69-605, AIAA 4th Thermophysics Conference, San Francisco, CA, June 16-18, 1969.

43. Hurwitz, F. I., Guo, H., Rogers, R. B., Olson, N., and Garg, A., "High Temperature Oxide Aerogels," *Springer Handbook of Aerogels*, Springer, Cham, 2023, pp. 437- 458. doi.org/10.1007/978-3-030-27322-4_18

44. Coleman, H. W., and Steele, W. G., *Experimentation and Uncertainties for Engineers*, Wiley, New York, 1989.

45. Blosser, M. L., "Mass Efficiency Considerations for Thermally Insulated Structural Skin of an Aerospace Vehicle," *Journal of Thermophysics and Heat Transfer*, Vol. 27, No. 3, July-September 2013, pp 429-434. doi.org/10.2514/1.T4008

46. Gembarovic, J., "Thermophysical Properties of Zirconia Insulation (Below RT)," TPRL 4512, June 2010.

47. Touloukian, Y. S., and Buyco, E. H., *Specific Heat, Nonmetallic Solids*, Vol. 5, Thermophysical Properties of Matter, IFI/Plenum, New York-Washington, 1970

48. Popov, P. A., Solomennik, V. D., Lomonova, E. E., Borik, M. A., and Myzinia, V. A., "Thermal Conductivity of Single Crystal ZrO_2-Y_2O_3 Solid Solutions in the Temperature Range 50-300 K," Physics of Solid State, Vol. 54, No. 3, 2012, pp. 658-661. doi.org/10.1134/S1063783412030250

49. Haupt, R. L., and Haupt, S. E., *Practical Genetic Algorithms*, Wiley, Hoboken, 1998.

50. Frye, E., and Daryabeigi, K., "Thermal Property Estimation of Fibrous Insulation: Heat Transfer Modeling and the Continuous Genetic Algorithm," AIAA Paper 2019-1279, AIAA SciTech Forum, San Diego, CA, 2019. doi.org/10.2514/6.2019-1279

51. Gembarovic, J., Freeman, J., and Taylor, D. L., "Thermophysical Properties of Two Materials," TPRL 4443c, February 2010.

52. Xie, Z., Xue, W., Chen, H., and Huang, Y., "Mechanical and Thermal Properties of 99% and 92% Alumina at Cryogenic Temperatures," *Ceram. Int.*, Vol. 37, No. 7, 2011, pp. 2165–2168. doi.org/10.1016/j.ceramint.2011.03.066

53. Kita, J., Engelbrecht, A., Schubert, F., Groß, A., Rettig, F., and Moos, R., "Some Practical Points to Consider with Respect to Thermal Conductivity and Electrical Resistivity of Ceramic Substrates for High-temperature Gas Sensors," *Sensor. Actuator. B Chem.,* Vol. 213, 2015, pp. 541–546. doi.org/10.1016/j.snb.2015.01.041

54. Gembarovic, J., and Freeman, J., "Thermophysical Properties of APA," TPRL 4473, March 2010.

55. Gembarovic, J., and Larsen, R., "Thermophysical Properties of Saffil Sample," TPRL 3911, October 2007.

Appendix

The various tabulated data are presented in this Appendix.

Table 1. Temperature and integrated thermal conductivity data at 0.001 torr for ZYF sample (LaRC Test 601).

	$L_i/L=1$			$L_i/L=0.727$		$L_i/L=0.454$		$L_i/L=0.182$	
T_C (K)	T_H (K)	$k_{int,1}$ (W.m^{-1}.K^{-1})	$\Delta k_{int,U}$ (%)	T_3 (K)	$k_{int,3}$ (W.m^{-1}.K^{-1})	T_2 (K)	$k_{int,2}$ (W.m^{-1}.K^{-1})	T_1 (K)	$k_{int,1}$ (W.m^{-1}.K^{-1})
282.7	535.8	0.0071	9.1	482.0	0.0066	420.1	0.0060	345.4	0.0052
283.2	817.2	0.0114	8.3	740.3	0.0097	626.8	0.0080	467.2	0.0060
284.1	1092.5	0.0186	6.5	1002.7	0.0152	855.9	0.0119	634.1	0.0078
284.1	1369.1	0.0296	5.3	1268.4	0.0237	1092.6	0.0180	826.0	0.0108
285.2	1505.2	0.0377	5.1	1410.0	0.0297	1217.9	0.0224	932.1	0.0129
286.6	1640.2	0.0481	4.9	1563.4	0.0371	1352.3	0.0278	1036.8	0.0158

Table 2. Thermal conductivity of ZYF (ρ = 289 kg.m^{-3}) as a function of temperature and pressure in dry air.

	Thermal Conductivity (W.m^{-1}.K^{-1}) at various Pressures (torr)								
T (K)	*P*=0.001	*P*=0.0076	*P*=0.076	*P*=0.76	*P*=3.8	*P*=7.6	*P*=38	*P*=76	*P*=760
300	0.0047	0.0048	0.0061	0.0143	0.0241	0.0270	0.0299	0.0303	0.0307
400	0.0069	0.0070	0.0083	0.0169	0.0296	0.0338	0.0385	0.0392	0.0398
500	0.0091	0.0093	0.0104	0.0193	0.0342	0.0398	0.0465	0.0475	0.0485
600	0.0118	0.0119	0.0130	0.0220	0.0388	0.0457	0.0544	0.0558	0.0572
700	0.0151	0.0152	0.0164	0.0254	0.0437	0.0519	0.0627	0.0646	0.0663
800	0.0196	0.0197	0.0208	0.0299	0.0495	0.0588	0.0719	0.0741	0.0763
900	0.0256	0.0257	0.0268	0.0359	0.0565	0.0669	0.0821	0.0849	0.0875
1000	0.0334	0.0335	0.0346	0.0436	0.0652	0.0766	0.0939	0.0971	0.1002
1100	0.0434	0.0435	0.0446	0.0535	0.0758	0.0881	0.1074	0.1111	0.1148
1200	0.0560	0.0561	0.0571	0.0660	0.0889	0.1019	0.1231	0.1273	0.1314
1300	0.0715	0.0716	0.0726	0.0814	0.1046	0.1183	0.1414	0.1460	0.1507
1400	0.0902	0.0903	0.0913	0.1001	0.1236	0.1379	0.1628	0.1679	0.1731
1500	0.1127	0.1128	0.1137	0.1224	0.1462	0.1611	0.1878	0.1934	0.1991
1600	0.1391	0.1392	0.1402	0.1487	0.1729	0.1884	0.2171	0.2232	0.2296
1700	0.1699	0.1700	0.1710	0.1794	0.2040	0.2203	0.2515	0.2583	0.2655

Table 3. Cryogenic thermal conductivity of ZYF (ρ = 251 kg.m^{-3}) in vacuum from Ref. 46.

T (K)	*k* (W.m^{-1}.K^{-1})
90.16	0.00257
110.16	0.00328
130.16	0.00394
180.16	0.00503
230.01	0.00579

Table 4. Thermal Conductivity of APA ($\rho = 98.4$ kg.m^{-3}) as a function of temperature and pressure in dry air.

T (K)	Thermal Conductivity (W.m^{-1}.K^{-1}) at various Pressures (torr)								
	P=0.001	*P=0.0076*	*P=0.076*	*P=0.76*	*P=3.8*	*P=7.6*	*P=38*	*P=76*	*P=760*
300	0.0040	0.0041	0.0049	0.0110	0.0209	0.0245	0.0287	0.0293	0.0299
400	0.0079	0.0079	0.0087	0.0150	0.0270	0.0321	0.0387	0.0397	0.0408
500	0.0120	0.0121	0.0129	0.0192	0.0327	0.0392	0.0482	0.0498	0.0513
600	0.0171	0.0172	0.0179	0.0242	0.0389	0.0466	0.0582	0.0603	0.0624
700	0.0237	0.0237	0.0244	0.0307	0.0464	0.0552	0.0693	0.0720	0.0747
800	0.0323	0.0324	0.0331	0.0393	0.0557	0.0655	0.0821	0.0855	0.0889
900	0.0436	0.0437	0.0443	0.0505	0.0675	0.0782	0.0973	0.1012	0.1054
1000	0.0581	0.0582	0.0589	0.0650	0.0825	0.0939	0.1153	0.1199	0.1248
1100	0.0766	0.0766	0.0773	0.0833	0.1011	0.1132	0.1368	0.1421	0.1477
1200	0.0994	0.0995	0.1001	0.1061	0.1241	0.1367	0.1623	0.1683	0.1746
1300	0.1273	0.1274	0.1280	0.1339	0.1521	0.1651	0.1926	0.1991	0.2062
1400	0.1608	0.1609	0.1615	0.1673	0.1856	0.1990	0.2283	0.2354	0.2433
1500	0.2006	0.2006	0.2012	0.2070	0.2253	0.2391	0.2701	0.2779	0.2866
1600	0.2471	0.2472	0.2478	0.2534	0.2718	0.2860	0.3190	0.3276	0.3372
1700	0.3011	0.3011	0.3017	0.3073	0.3258	0.3404	0.3759	0.3853	0.3962

Table 5. Cryogenic thermal conductivity of APA ($\rho = 112$ kg.m^{-3}) in vacuum from Ref. 51.

T (K)	k (W.m^{-1}.K^{-1})
130.16	0.000995
180.16	0.001379
223.16	0.001773
273.16	0.002428

Table 6. Thermal Conductivity of OFI (ρ = 99.2 kg.m^{-3}) as a function of temperature and pressure in dry air.

	Thermal Conductivity (W.m^{-1}.K^{-1}) at various Pressures (torr)								
T (K)	*P*=0.001	*P*=0.0076	*P*=0.076	*P*=0.76	*P*=3.8	*P*=7.6	*P*=38	*P*=76	*P*=760
300	0.0023	0.0024	0.0038	0.0124	0.0221	0.0248	0.0275	0.0279	0.0283
400	0.0051	0.0053	0.0066	0.0157	0.0283	0.0324	0.0368	0.0375	0.0381
500	0.0088	0.0089	0.0102	0.0195	0.0345	0.0399	0.0463	0.0472	0.0482
600	0.0134	0.0135	0.0147	0.0242	0.0411	0.0479	0.0562	0.0575	0.0588
700	0.0190	0.0191	0.0203	0.0298	0.0484	0.0564	0.0668	0.0685	0.0702
800	0.0256	0.0258	0.0269	0.0365	0.0565	0.0657	0.0782	0.0803	0.0824
900	0.0335	0.0337	0.0348	0.0444	0.0655	0.0758	0.0904	0.0930	0.0955
1000	0.0427	0.0429	0.0440	0.0536	0.0757	0.0869	0.1036	0.1066	0.1096
1100	0.0534	0.0535	0.0546	0.0641	0.0870	0.0992	0.1178	0.1213	0.1247
1200	0.0655	0.0656	0.0667	0.0761	0.0996	0.1126	0.1332	0.1371	0.1410
1300	0.0792	0.0793	0.0804	0.0897	0.1137	0.1274	0.1497	0.1541	0.1585
1400	0.0946	0.0947	0.0958	0.1050	0.1294	0.1437	0.1678	0.1726	0.1775
1500	0.1119	0.1120	0.1130	0.1222	0.1468	0.1618	0.1877	0.1930	0.1984
1600	0.1310	0.1311	0.1321	0.1412	0.1662	0.1818	0.2097	0.2156	0.2216
1700	0.1522	0.1523	0.1533	0.1622	0.1877	0.2041	0.2345	0.2410	0.2478
1800	0.1754	0.1755	0.1765	0.1854	0.2115	0.2289	0.2626	0.2701	0.2779
1900	0.2008	0.2009	0.2019	0.2108	0.2377	0.2564	0.2947	0.3036	0.3131

Table 7. Thermal Conductivity of APA2-AS (ρ = 148.2 kg.m^{-3}) as a function of temperature and pressure in dry air.

T (K)	Thermal Conductivity (W.m^{-1}.K^{-1}) at various Pressures (torr)								
	P=0.001	P=0.0076	P=0.076	P=0.76	P=3.8	P=7.6	P=38	P=76	P=760
300	0.0053	0.0053	0.0053	0.0053	0.0055	0.0056	0.0069	0.0083	0.0201
400	0.0068	0.0068	0.0068	0.0069	0.0070	0.0072	0.0084	0.0098	0.0232
500	0.0095	0.0095	0.0095	0.0095	0.0096	0.0098	0.0110	0.0124	0.0268
600	0.0137	0.0137	0.0137	0.0137	0.0138	0.0140	0.0151	0.0165	0.0317
700	0.0198	0.0198	0.0198	0.0198	0.0200	0.0201	0.0212	0.0225	0.0383
800	0.0284	0.0284	0.0284	0.0284	0.0285	0.0287	0.0297	0.0311	0.0472
900	0.0398	0.0398	0.0398	0.0398	0.0399	0.0401	0.0411	0.0424	0.0589
1000	0.0545	0.0545	0.0545	0.0546	0.0547	0.0548	0.0559	0.0571	0.0738
1100	0.0730	0.0730	0.0730	0.0731	0.0732	0.0733	0.0743	0.0756	0.0924
1200	0.0957	0.0957	0.0957	0.0958	0.0959	0.0960	0.0970	0.0983	0.1151
1300	0.1231	0.1231	0.1231	0.1231	0.1232	0.1233	0.1243	0.1256	0.1424
1400	0.1555	0.1555	0.1555	0.1556	0.1557	0.1558	0.1568	0.1580	0.1748

Table 8. Thermal Conductivity of Saffil (ρ = 48 kg.m^{-3}) as a function of temperature and pressure in dry air.

T (K)	Thermal Conductivity (W.m^{-1}.K^{-1}) at various Pressures (torr)								
	P=0.001	P=0.0076	P=0.076	P=0.76	P=3.8	P=7.6	P=38	P=76	P=760
300	0.0029	0.0032	0.0055	0.0166	0.0250	0.0268	0.0285	0.0287	0.0289
400	0.0088	0.0091	0.0113	0.0237	0.0354	0.0383	0.0411	0.0415	0.0418
500	0.0166	0.0168	0.0190	0.0322	0.0468	0.0508	0.0549	0.0555	0.0560
600	0.0267	0.0269	0.0290	0.0428	0.0601	0.0652	0.0706	0.0714	0.0722
700	0.0397	0.0399	0.0420	0.0561	0.0758	0.0821	0.0890	0.0900	0.0910
800	0.0561	0.0563	0.0584	0.0728	0.0946	0.1020	0.1105	0.1117	0.1129
900	0.0766	0.0768	0.0788	0.0934	0.1170	0.1256	0.1356	0.1372	0.1386
1000	0.1015	0.1017	0.1037	0.1185	0.1438	0.1534	0.1650	0.1668	0.1685
1100	0.1316	0.1318	0.1337	0.1486	0.1752	0.1859	0.1990	0.2011	0.2031
1200	0.1673	0.1675	0.1694	0.1842	0.2121	0.2236	0.2383	0.2407	0.2430
1300	0.2092	0.2094	0.2112	0.2260	0.2549	0.2673	0.2834	0.2861	0.2887
1400	0.2578	0.2580	0.2598	0.2745	0.3042	0.3175	0.3351	0.3380	0.3409

Table 9. Thermal Conductivity of Saffil ($\rho = 96$ kg.m^{-3}) as a function of temperature and pressure in dry air.

T (K)	Thermal Conductivity (W.m^{-1}.K^{-1}) at various Pressures (torr)								
	$P=0.001$	$P=0.0076$	$P=0.076$	$P=0.76$	$P=3.8$	$P=7.6$	$P=38$	$P=76$	$P=760$
300	0.0015	0.0016	0.0028	0.0108	0.0206	0.0235	0.0266	0.0270	0.0274
400	0.0044	0.0045	0.0057	0.0141	0.0267	0.0310	0.0359	0.0367	0.0374
500	0.0083	0.0084	0.0095	0.0181	0.0328	0.0386	0.0455	0.0466	0.0477
600	0.0133	0.0135	0.0145	0.0231	0.0397	0.0467	0.0558	0.0573	0.0588
700	0.0198	0.0199	0.0210	0.0296	0.0477	0.0559	0.0672	0.0692	0.0710
800	0.0281	0.0282	0.0292	0.0379	0.0571	0.0665	0.0800	0.0824	0.0848
900	0.0383	0.0384	0.0394	0.0480	0.0683	0.0788	0.0945	0.0974	0.1002
1000	0.0508	0.0509	0.0519	0.0605	0.0816	0.0930	0.1109	0.1142	0.1176
1100	0.0658	0.0659	0.0669	0.0754	0.0972	0.1095	0.1294	0.1332	0.1371
1200	0.0837	0.0837	0.0847	0.0932	0.1154	0.1285	0.1503	0.1547	0.1591
1300	0.1046	0.1047	0.1056	0.1140	0.1366	0.1503	0.1740	0.1789	0.1838
1400	0.1289	0.1290	0.1299	0.1382	0.1611	0.1754	0.2009	0.2062	0.2117

Table 10. Pertinent data for the various insulation materials.

Sample	Test No.	ρ_s (kg.m^{-3})	f	κ (m)	k_{LP}	F	$e/n*^2$
ZYF	601	289	0.0515	1.29×10^{-4}	Eq. 23	4.793×10^{-2}	Eq. 28b
APA	602	98.4	0.0308	8.16×10^{-5}	Eq. 30	5.676×10^{-4}	Eq. 33b
OFI	603	99.2	0.0311	1.38×10^{-4}	Eq. 34	---	---
APA2-AS	612	148.2	0.0479	2.885×10^{-7}	Eq. 35	---	---
Saffil		48	0.0147	2.43×10^{-4}	Eq. 36	---	---